BIOPHYSICS

Flies land upside down on a ceiling using rapid visually mediated rotational maneuvers

Pan Liu[1], Sanjay P. Sane[2], Jean-Michel Mongeau[1], Jianguo Zhao[3], Bo Cheng[1]*

Flies and other insects routinely land upside down on a ceiling. These inverted landing maneuvers are among the most remarkable aerobatic feats, yet the full range of these behaviors and their underlying sensorimotor processes remain largely unknown. Here, we report that successful inverted landing in flies involves a serial sequence of well-coordinated behavioral modules, consisting of an initial upward acceleration followed by rapid body rotation and leg extension, before terminating with a leg-assisted body swing pivoted around legs firmly attached to the ceiling. Statistical analyses suggest that rotational maneuvers are triggered when flies' relative retinal expansion velocity reaches a threshold. Also, flies exhibit highly variable pitch and roll rates, which are strongly correlated to and likely mediated by multiple sensory cues. When flying with higher forward or lower upward velocities, flies decrease the pitch rate but increase the degree of leg-assisted swing, thereby leveraging the transfer of body linear momentum.

INTRODUCTION

Flies are agile small fliers that routinely perform a wide variety of aerodynamic feats (*1*–*3*). Among these, landing upside down on a ceiling (i.e., inverted landing) (*4*) is arguably among the most difficult and least understood aerobatic maneuver. Inverted landing requires small fliers, whether robotic or biological, to rapidly coordinate distance, velocity, and body orientation, using simple but fast sensorimotor processing. Smaller fliers also rely more on passive mechanical and structural processes, for their favored size dependency (*5*, *6*), to partially alleviate the demand on sensing and computation. In particular, flies landing on vertical (*7*, *8*) or inverted (*4*, *9*, *10*) surfaces use their extended legs to assist a body swing, or a "cartwheel," to align their body with the landing surface. This process relies heavily on the adhesion from cushion-like pads on their feet (called pulvilli) (*11*), which ensures a firm grip, and the viscoelasticity of the compliant leg joints, which damps out impact upon contact (*7*, *9*). Visual computation then acts in concert with these mechanical adaptations and initiates the leg extension (*12*) that is commonly considered stereotyped (*13*). Thus, for a successful landing, flies and other insects may not need to actively adjust their body orientation (via a controlled body rotational maneuver) immediately before the touchdown (i.e., when tarsi touch the substrate).

However, past research on inverted landing suggests that flies sometimes exhibit and, therefore, are at least capable of generating rapid rotational maneuvers immediately before touchdown. For example, Hyzer (*4*) described that flies (*Musca domestica*) occasionally performed a "half-roll" body rotation before touching the ceiling with their ipsilateral feet; this was followed by a lateral leg-assisted body swing that brought the other four feet into contact with the ceiling. Recent observations on inverted landing (*9*) showed that flies (*M. domestica*) actively pitched up their body before contacting the ceiling, sometimes using a combination of roll, pitch, and yaw body rotation. These observations, albeit limited, suggest that rapid body rotational maneuver may be a critical yet versatile component of the inverted landing behaviors. Moreover, their patterns are also likely mediated by visual and other sensory processes immediately before the touchdown.

In this study, we investigated the inverted landing behaviors of blue bottle flies (*Calliphora vomitoria*) in a flight chamber using high-speed videography (Fig. 1A). The kinematics of the flies' body and wing were extracted through digitization of anatomical landmarks (Fig. 1, B and C). First, we describe the sequential behavioral modules of the inverted landing, along with the kinematic variations in successful landings, and differences between successful and failed landings. We next show that the rotational maneuvers, occurring immediately before the touchdown, are triggered by retinal expansion. Their peak pitch and roll rates are correlated with and therefore likely mediated by multiple sensory cues. Last, we quantify the changes of wing kinematic patterns that generate these rotational maneuvers. Our study provides critical insights on inverted landing behaviors and the underlying biomechanical, sensory, and neural processes. It also points to possible mechanisms that can enable small-animal or robotic systems with limited computational resources to generate fast yet complex behaviors.

RESULTS

Behavioral modules in successful inverted landing

Fruit flies (*Drosophila*) land on vertical surfaces by continuous deceleration with negligible body rotation before the touchdown (*8*, *14*). In contrast, blue bottle flies (*Calliphora*) landing on a ceiling exhibited a sequence of four behavioral modules—started with an upward acceleration, followed by a rapid body rotational maneuver and leg extension, and ended with a leg-assisted body swing with forelegs firmly planted on the ceiling, thereby orienting the fly's body ventral side up (i.e., inverted) (Fig. 1 and fig. S3, Aii and Bii). The process from the start of the body rotation to the ventral side up landing lasted approximately four to eight wingbeats in all the successful landings (n = 18; table S1) (average wingbeat frequency, 172.7 ± 7.7 Hz).

In successful inverted landings, we observed substantial kinematic variations in the axes of rotation and the magnitude of rotational maneuvers, as well as in the degree of leg-assisted body swing. Thus, flies used a wide range of maneuvers when landing on a ceiling, which we categorized into pitch dominated, roll dominated, pitch and roll combined, and longitudinal or lateral body swing dominated (movie S1 to S5 and table S1). Examples of three typical sequences are shown

[1]Department of Mechanical Engineering, Pennsylvania State University, University Park, PA 16802, USA. [2]National Centre for Biological Sciences (NCBS), Tata Institute of Fundamental Research, GKVK Campus, Bellary Road, Bangalore 560065, India. [3]Department of Mechanical Engineering, Colorado State University, Fort Collins, CO 80523, USA.
*Corresponding author. Email: buc10@psu.edu

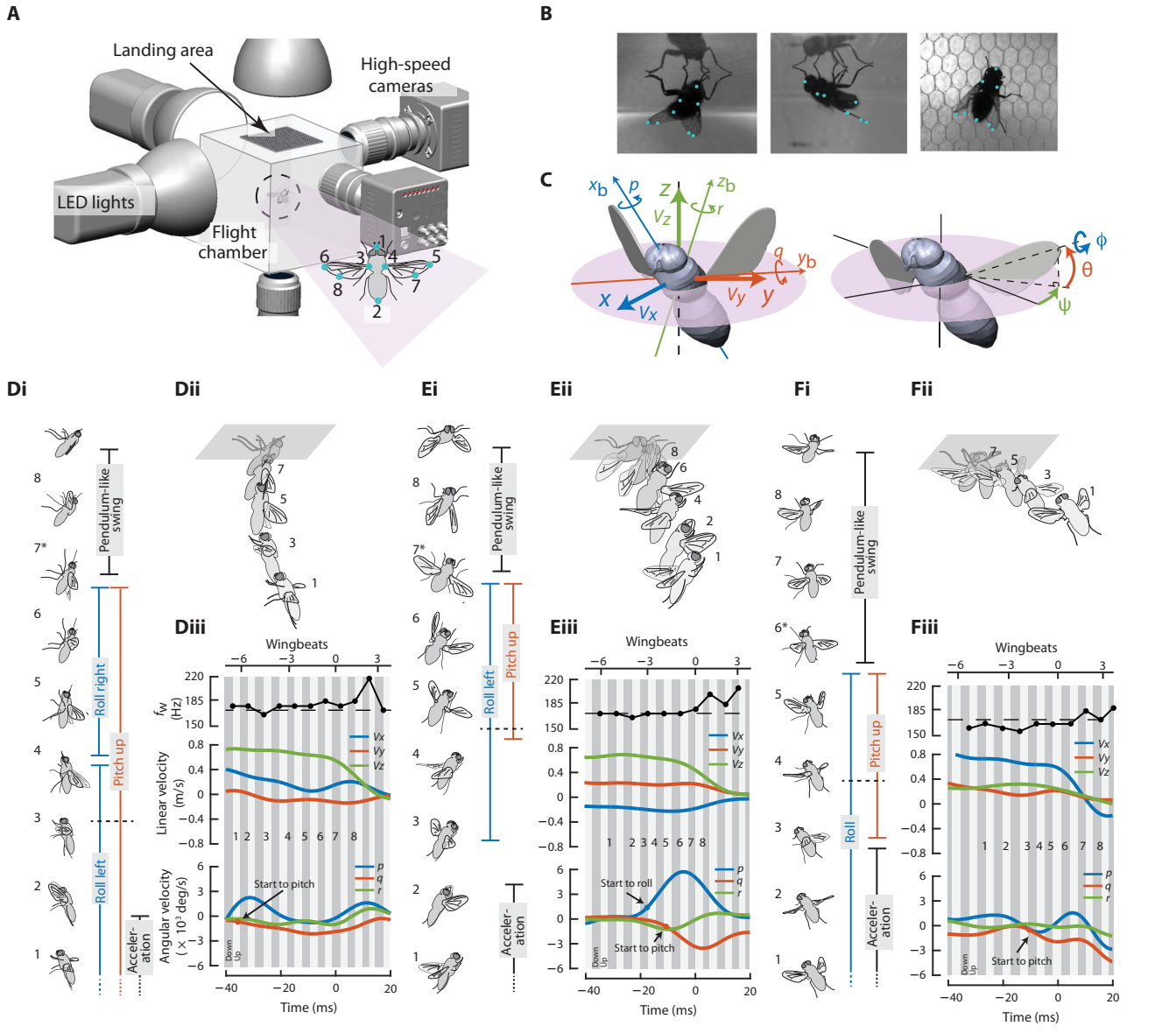

Fig. 1. Experimental setup, kinematic definitions, and some examples of diverse inverted landing sequences. (**A**) Landing maneuvers of flies are captured by three high-speed cameras operating at 5000 frames/s with exposure of 1/25,600 s. The landing area (10 cm by 10 cm) is located at the center of the ceiling of the flight chamber (20 cm by 20 cm by 20 cm) and is covered by mesh patterns to enhance visual contrast. (**B**) Anatomical landmarks of the flies from the captured images are digitized, from which we determine the body and wing kinematics according to the coordinate systems and kinematic angles defined in (C). (**C**) Body rotation is defined with respect to the body-fixed frame $\mathcal{F}_b = \{x_b, y_b, z_b\}$, where angular velocity is represented by roll p, pitch q, and yaw r rates. Body translational velocity relative to the ceiling is calculated with respect to the yaw-aligned global frame $\mathcal{F} = \{x, y, z\}$, which is obtained via rotating the global frame by the fly's yaw angle. The translational velocity is represented by forward/aft V_x, lateral V_y, and vertical V_z components. Wing kinematics are described by three Euler angles: stroke ψ, deviation θ, and rotation ϕ. The inverted landing behaviors are exemplified by those with rapid rotational maneuvers primarily about (**D**) pitch or (**E**) roll axes, and (**F**) those with a large leg-assisted body swing. (i) Sketches of flight sequences are separated spatially to make each instance visible. The instant when flies start to extend forelegs is denoted by the horizontal black dash line. (ii) Sketches of flight sequences are shown in their actual relative spatial locations. (iii) The time traces of wingbeat frequency f_w; body translational velocities V_x, V_y, and V_z; and body angular velocities p, q, and r. The time 0 represents the instant when a fly's leg first touches the ceiling, which is also indicated by the asterisk in (i). Black dashed lines in the subplots of f_w denote the average wingbeat frequency of the reference wing kinematics (173 Hz), measured during the upward-acceleration phase prior to the rotational maneuvers. The time instants starting to pitch or roll are identified separately as the instants when the pitch or roll rate reaches one-fourth of the corresponding peak rate. In comparison to (D) and (E), where flies maintain high upward velocities V_z (~0.8 m/s) and reach nearly ventral side up orientations by actively generating rapid pitch or roll maneuvers, the landing maneuver exemplified in (F) is characterized with large forward velocity V_x and negligible body rotational maneuver before forelegs touchdown. (Photo credit: Bo Cheng, Pennsylvania State University.)

in Fig. 1 (D to F), illustrating parts of this variation. In the first two examples, flies used rapid rotational maneuvers primarily about pitch (Fig. 1D and movie S1) or roll (Fig. 1E and movie S2), which oriented their body to a nearly inverted orientation before touchdown. Leg extension occurred slightly after the start of the rotational maneuvers (horizontal black dashed lines, Fig. 1, Di and Ei), and the body swinging phase followed after legs were planted on the substrate. Notably, the average peak angular rate of the rotational maneuvers reached approximately

4000°/s (fig. S3, Av and Bv) and could be as high as 6000°/s (Fig. 1Eiii), greater than those reported in the escape maneuvers of fruit flies (*1*) and hummingbirds (*15*). In the third example, flies relied almost entirely on the leg-assisted body swing to reorient and landed with negligible rotational maneuver (Fig. 1F and movie S3), similar to previously reported landing on vertical surfaces (*4*, *8*). Thus, compared with the first two, this landing strategy likely leveraged more of the mechanical and structural processes (e.g., adhesion due to pulvilli or damping due to viscoelasticity of leg) (*16*), which assisted the transfer of the body's linear momentum to rotational momentum.

Kinematic differences between successful and failed landings

We observed both successful and failed landings. A subset of flies landed in a smooth and coordinated fashion (successful landings), whereas others failed to land properly and collided head-on upon approach (failed landings). In successful landings, the four behavioral modules collectively led to a proper combination of body inversion and linear velocity with properly positioned legs prior to touchdown.

To quantify how well a fly's body was oriented, we calculated the degree of inversion (DoI), which measures the degree to which the fly's body is aligned with respect to a fully inverted orientation before touchdown (see Materials and Methods). DoI ranges from 0, representing no body inversion (or ventral-side down), to 1, representing full body inversion (or ventral-side up). In successful landings, the DoI increased with vertical velocity (Fig. 2A) but decreased with the forward velocity (Fig. 2B). This indicated that flies needed to be more inverted when their upward velocity was greater or when their horizontal velocity was lower. In most failed landings (total $N = 15$ analyzed; table S1), the flies were insufficiently inverted before touchdown, as compared with successful landings (Fig. 2). The failure in these landings can be attributed to delayed or minor body rotation prior to touchdown (Supplementary Materials). Consequently, these flies could not properly land on the ceiling but instead collided head-on. Notably, flies also failed at landing due to early rotation (see movie 7), as the early inversion led to insufficient vertical velocity to reach the ceiling ("+" in Fig. 2). Last, in some failed landings, flies had similar inversion to that of successful landings, but failed regardless. This happened due to delayed leg extension, which resulted in an improperly positioned leg to have the tarsi firmly planted on the substrate (see movie 8).

Yet, even after failed attempts, flies could still recover and land, using groping landing ($n = 24$; table S1). In this type of inverted landing, flies hover or fly at low vertical speed underneath the ceiling (Fig. 2), then they grope for the ceiling using their forelegs, and with a firm grip on the substrate, swing their body up to land (movie S6).

The kinematic complexities and variations in inverted landings indicate that they may involve more diverse neural processes than those reported for triggering leg extension and deceleration (*8*, *12*, *14*). In particular, the rotational maneuver with variable pitch and roll for a proper inversion was the major determining factor for success. Thus, in addition to being triggered, it is likely that the rotational maneuvers were mediated by sensory cues in a short period immediately before touchdown. We next examined the potential sensory cues and their roles in triggering and mediating the rotational maneuvers, based on the statistical analyses of the kinematic data.

Triggering of rotational maneuvers

We first describe the putative visual cues that flies could sense as they approach the ceiling with three components of linear velocity (vertical V_z, fore/aft V_x, and lateral V_y; Fig. 1C). Note that our study does not

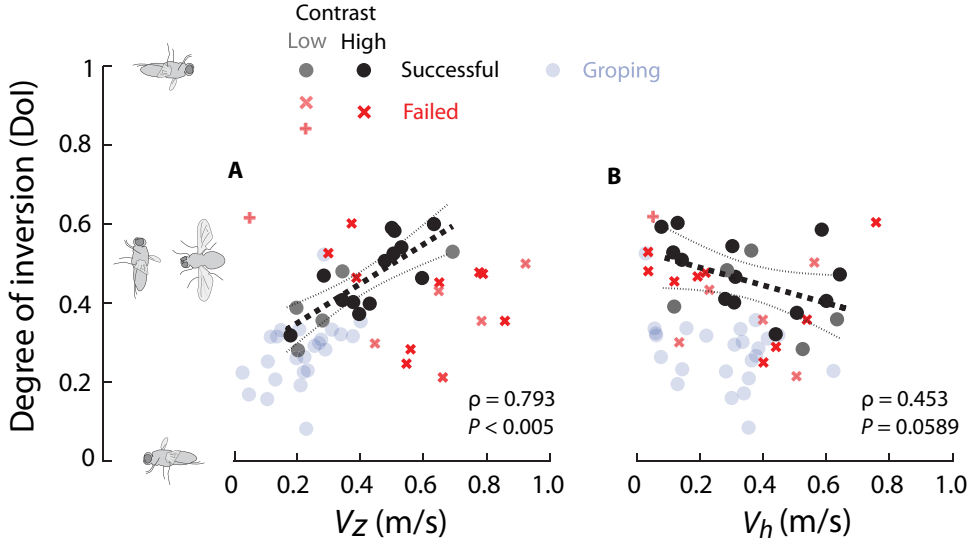

Fig. 2. DoI of the flies' body depended on the vertical and horizontal velocity components shortly before the feet touchdown in successful landing. For successful, groping, and failed landing cases, the DoI of flies' body are plotted against the vertical (V_z) and horizontal (V_h) components of flies' body linear velocity one wingbeat before the feet touchdown. Successful landing cases are marked in black, failed landing in red, and groping landing in light blue. The failed landing cases due to low body inversion and early body rotation are marked as "×" and "+," respectively. (**A**) DoI versus V_z and (**B**) DoI versus V_h. The highest V_z observed among successful landings is approximately 0.7 m/s. DoI ranges from 0, representing no body inversion (or ventral side down), to 1, representing full body inversion (or ventral side up). DoI increases with V_z but decreases with V_h in successful landing cases. For successful landings, the linear regressions between DoI and V_z, and DoI and V_h are shown with the Pearson's linear correlation coefficient ρ and P value; the 95% confidence intervals are also shown. In general, failed landing cases have lower DoI and higher V_z than the successful landing. Groping landing cases have relatively low DoI and low vertical velocity. The successful landing cases for low- and high-contrast landing areas are also differentiated.

consider feature-related triggering (e.g., object retinal location) (*8*), because, ideally, the use of uniform mesh grids should generate coherent motion over the entire retina when the fly is sufficiently close to the ceiling. Previous work on insect visual control (*8*, *14*, *17*) emphasized the importance of three types of visual cues. First is the relative retinal expansion velocity (RREV) due to looming stimuli (Fig. 3), which can be calculated as the ratio of a target's expansion rate to its size on the fly retina during upward translation (V_z). RREV also corresponds to the reciprocal of a physical variable called time to collision τ, which represents the time to collision, assuming constant velocity (*14*). RREV is considered an important perceptual cue that controls the approaching velocity during landing or obstacle avoidance (*18*, *19*). Second is the relative fore/aft angular velocity (or translational optic flow) of the ceiling on the fly retina (ω_y) (Fig. 4Ai). These visual cues result from the body fore/aft translation (V_x) and were found previously to control the grazing landing on horizontal surfaces (*17*). Third is the relative lateral angular velocity (or translational optic flow) of the ceiling ω_x on the fly retina (Fig. 4Bi), resulting from lateral translation (V_y). We calculated the time traces of these three visual cues in both the yaw-aligned global frame and the retina-fixed frame (fig. S4) using kinematic variables according to their mathematical relationships (fig. S1). All three visual cues could be calculated directly from the optic flow [see Supplementary Materials and (*19*)].

We assumed that the rotational maneuvers were triggered after a fixed time delay when the triggering visual cue reached a threshold (*14*). This is arguably the most parsimonious predictive model for the triggering and enabled us to test whether the above visual cues are related to the onset of the rotational maneuvers as described below.

We calculated the time traces of the coefficient of variance (CV) for each visual cue using trials in which flies landed successfully in their first attempt on a high-contrast landing area (table S1). The results for the RREV are shown in Fig. 3, while the complete results are shown in figs. S4 and S5 (Supplementary Materials). The CV measures the dispersion of a variable defined by the ratio of its SD and mean. The triggering of the pitch and roll motion was analyzed separately by aligning data from different landing trials at either the start of the pitch or roll. If the rotational maneuvers were triggered after some time delay when a visual cue reached a threshold value, the CV of this visual cue should be at its minimum. In addition, it should be lower than those of other nontriggering visual cues (*14*), i.e., the triggering visual cue should have the least dispersion (see Materials and Methods). For example, in a previous study on the triggering of linear deceleration in houseflies (*Musca domestica* L.) landing on vertical posts (*14*), the CV of the RREV is approximately 30%, lower than the other variables. Here, among the three visual cues tested, the RREV in the yaw-aligned global frame had the least CV for triggering either pitch (15%) or roll (25%) rotations (Fig. 3B), whereas the CV of the other two visual cues were significantly larger (figs. S4, A to C, and S5, A to C). This indicated that RREV was the primary visual cue triggering rotational maneuvers in inverted landing, similar to the triggering of deceleration for landing on vertical posts. Note that the CV of distance between the fly and the ceiling was close to that of the RREV (figs. S4D and S5D); however, flies are thought to not be able to directly measure distance (*20*, *21*).

The CV of the RREV was minimum, approximately between 7 ms (ΔT_l) and 27 ms (ΔT_u) before the onset of rotational maneuvers (Fig. 3B), suggesting that the visual latency ΔT between the instant of perception and the onset of a maneuver was within this small range. Although the latency inferred from this analysis was smaller than estimated from other behavioral studies, e.g., in linear speed control (*22*) and escape maneuvers (*1*), it fell within the range of latency in a fly's visuomotor pathway (*23*, *24*). Last, the corresponding RREV threshold value (Fig. 3B) indicated that the critical time to collision, below which the rotational maneuver was likely to be triggered, was between 31 and 53 ms. This threshold is lower than the one previously identified for triggering the prelanding deceleration in houseflies landing on vertical posts, which was approximately 76 ms (*14*).

Sensory mediation of rotational maneuvering patterns

Rotational maneuvers were highly variable in terms of their roll and pitch rates, which in successful landing have led to a proper body

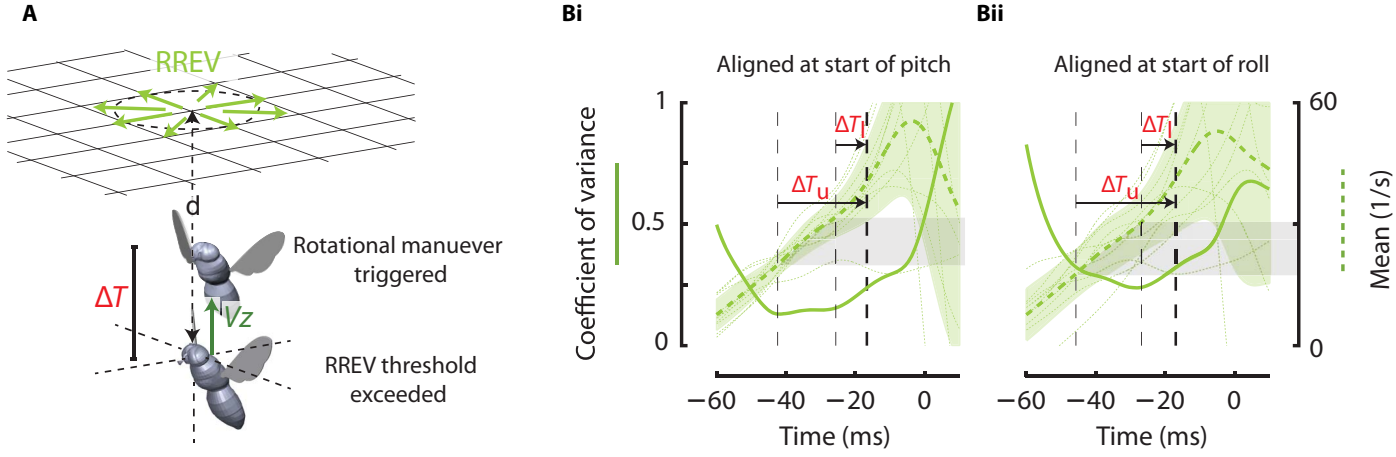

Fig. 3. The rotational maneuvers are triggered with short delays when RREV exceeds a threshold. (**A**) When a fly approaches the ceiling with velocity V_z, it perceives looming stimuli with increasing RREV on its retina. When RREV exceeds a threshold, the rotational maneuvers are triggered after a time delay ΔT. (**B**) Time traces of the coefficients of variation (CV) (thick solid green) and mean values (thick dashed green, the green shaded areas represent ±1 SD) of the RREV ($n = 10$). The time traces from the individual landing maneuvers (thin dotted green) are aligned at the instants when (Bi) the body pitch or (Bii) the body roll motion starts, as indicated by the thick black dashed lines. Time 0 indicates the averaged time instant when one of the fly's feet first touched the ceiling. The CV and mean values for the other estimated sensory cues are shown in figs. S4 and S5. To estimate the time delay ΔT, a time period when the CV of RREV reaches a low-value region is defined (between the two thin black dashed lines) (Supplementary Materials), the lower and upper bounds of which yield an upper bound (ΔT_u=27 ms) and a lower bound (ΔT_l = 7 ms) estimate of the time delay. The gray shaded areas represent the corresponding range of RREV threshold for triggering the rotational maneuver, which is between 19 and 32 rad/s, corresponding to time to collision between 53 and 31 ms, respectively.

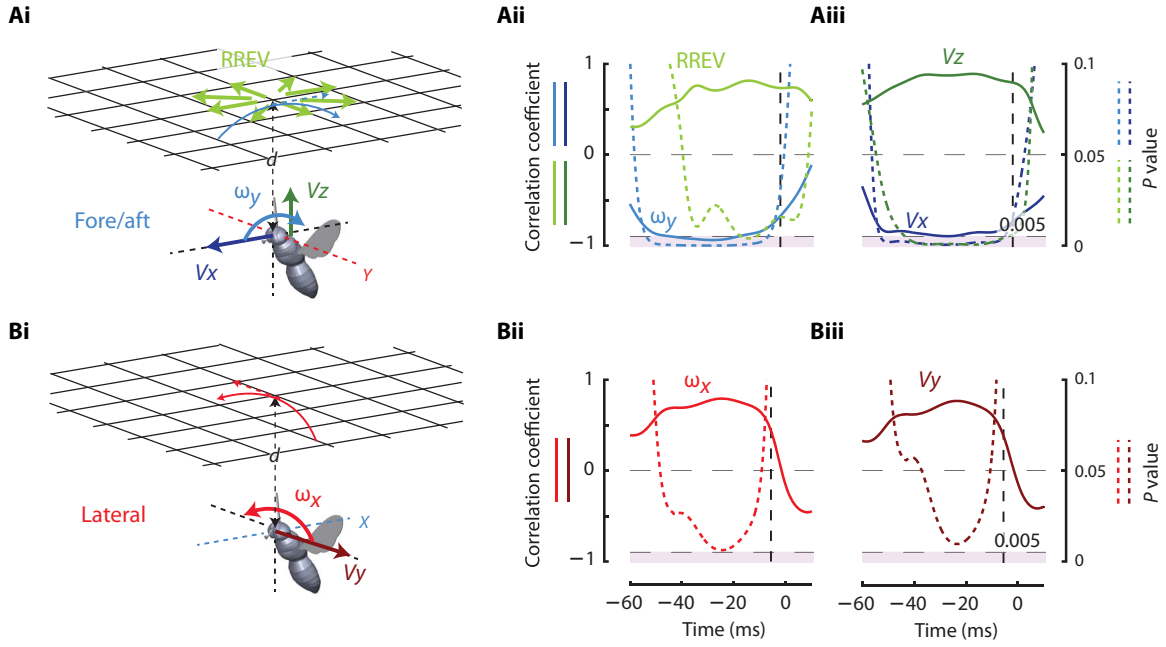

Fig. 4. The rotational maneuver patterns are correlated with multiple sensory cues perceived during inverted landing. (**Ai**) The fly's upward motion V_z results in RREV, and the fly's fore/aft motion V_x results in the ceiling rotating backward/forward on the fly's retina (ω_y about the *Y* axis). (**Bi**) Similarly, the fly's lateral motion V_y results in the ceiling rotating laterally (in an opposite direction) on the fly's retina (ω_x about the *X* axis). Among the successful landing trials, there exist strong correlations between peak pitch or roll rate and multiple sensory cues at different preceding time instants; the time traces of the corresponding correlation coefficients and the *P* value are shown for visual cues (Aii) ω_y, RREV and (Bii) ω_x, and mechanosensory cues (Aiii) V_x and V_z, and (Biii) V_y. As an example, fig. S8 shows the linear regressions between the peak pitch (or roll) rate with the visual cues at a particular preceding time instant (20 ms before the peak). The solid and dashed lines represent the Pearson's linear correlation coefficients and *P* value, respectively. The shaded areas indicate the region where $P \leq 0.005$. The peak pitch rate is positively correlated with RREV and V_z, and negatively correlated with ω_y and V_x. The peak roll rate is positively correlated with ω_x and V_y. All the time traces from different landing trials are aligned at the instant of peak pitch or roll rate, which is indicated by vertical black dashed lines. Time 0 indicates the averaged time instant when one of the fly's feet first touch the ceiling. The complete correlation results between the pitch (or roll) rate and the estimated sensory cues are shown in figs. S6 and S7 and table S2.

inversion according to the flies' body linear velocity (Fig. 2). This suggested that, in addition to the onset timings, the patterns of the rotational maneuvers were also mediated by sensory cues. Flies are known to use sensory cues to mediate rotational maneuvers via both feedforward and feedback pathways (*25*). The feedforward path issues spontaneous steering commands that produce large, transient wing motion changes, which determine the initial response magnitude of the maneuver (*25*, *26*). The feedback path mediates compensatory reaction (e.g., haltere-mediated feedback) that produces fine-scaled wing motion change, which determines the active damping and stabilizes the maneuver (*2*, *25*, *26*). Here, we identified the potential sensory cues and their roles in the feedforward mediation of the rotational maneuvers. This was achieved by identifying the correlations between the peak roll and pitch rates of the rotational maneuvers with the sensory cues perceived by flies prior to or slightly after the onset of the maneuvers. Note that these sensory cues were mainly dependent on the flies' body linear velocities shortly before the onset of rotational maneuvers, when body angular velocity was negligible.

Specifically, we evaluated correlations between the peak pitch and roll rates with a set of putative sensory cues at varying time instants prior to or slightly after the onset of rotational maneuvers (Fig. 4, and more details in figs. S6 and S7 and table S2). The correlations using the sensory cues 20 ms before the peak angular rates are shown in fig. S8 as an example. We used angular rates rather than angular acceleration because previous studies suggested that motor responses (i.e., wing kinematic control variables) were more strongly correlated with body angular rates due to the periodic and highly damped nature of flapping flight (*27*, *28*). The putative sensory cues included the three visual cues tested above for the triggering (RREV, ω_x, and ω_y) and the three components of body linear velocity (V_x, V_y, and V_z), which were likely perceived via mechanosensory modalities of flies (*29*). Linear regression analysis showed that, within a large time period prior to the onset of the maneuvers ($P < 0.05$, Student's *t* test), the peak pitch rate was positively correlated with RREV (Fig. 4Aii) and vertical velocity V_z (Fig. 4Aiii), but negatively correlated with fore/aft ceiling rotation ω_y (Fig. 4Aii) and fore-aft linear velocity V_x (Fig. 4Aiii). Similarly, peak roll rates were positively correlated with the lateral ceiling rotation ω_x (Fig. 4Bii) and lateral linear velocity V_y (Fig. 4Biii), also within a large period ($P < 0.05$, Student's *t* test) prior to or shortly after the onset of the maneuvers. The above correlation analysis supports the possibility of sensory mediation of rotational maneuver patterns, with pitch mediated by sensory cues encoding upward and fore/aft translation, and roll mediated by sensory cues encoding lateral translation.

The above correlation analysis also raised the possibility that flies modulate the magnitude of rotational maneuvers to exploit leg-assisted body swing, including transfer of linear to angular momentum. Specifically, flies exhibited a reduced pitch rate when forward linear momentum was high, as indicated by the negative correlation between peak pitch rate with sensory cues resulting from forward translation (visual ω_y or mechanosensory V_x). Thus, instead of active pitching, flies inverted their body by increasing the leg-assisted longitudinal body swing and the transfer of forward linear momentum to pitch angular

momentum (Fig. 1F). On the other hand, flies exhibited an increased roll rate when the lateral linear momentum was high, as indicated by the positive correlation between peak roll rate and sensory cues resulting from lateral translation (visual ω_x or mechanosensory V_y). This opposite correlation may result if flies need sufficiently large banking to raise their ipsilateral legs high enough to reach the ceiling for the leg-assisted body swings (middle legs cannot extend upward as high as forelegs without banking the fly's body). Thus, this strategy could also assist the execution of lateral body swings that transferred lateral linear momentum to roll angular momentum.

Wing kinematic patterns that produce pitch and roll

The execution of the rotational maneuvers requires sensorimotor transduction of sensory cues to motor outputs that help modulate wing motion to generate various aerodynamic forces and moments. We next examined the changes of wing motion responsible for generating pitch and roll during rotational maneuvers. The wing motion patterns underwent moderate changes that lie between those reported in fruit flies (*1*) and hummingbirds (*27*) during escape maneuvers. We observed the following changes. First are the bilaterally symmetric changes in wing spanwise rotation (Fig. 5, A and Ci) and bilaterally symmetric

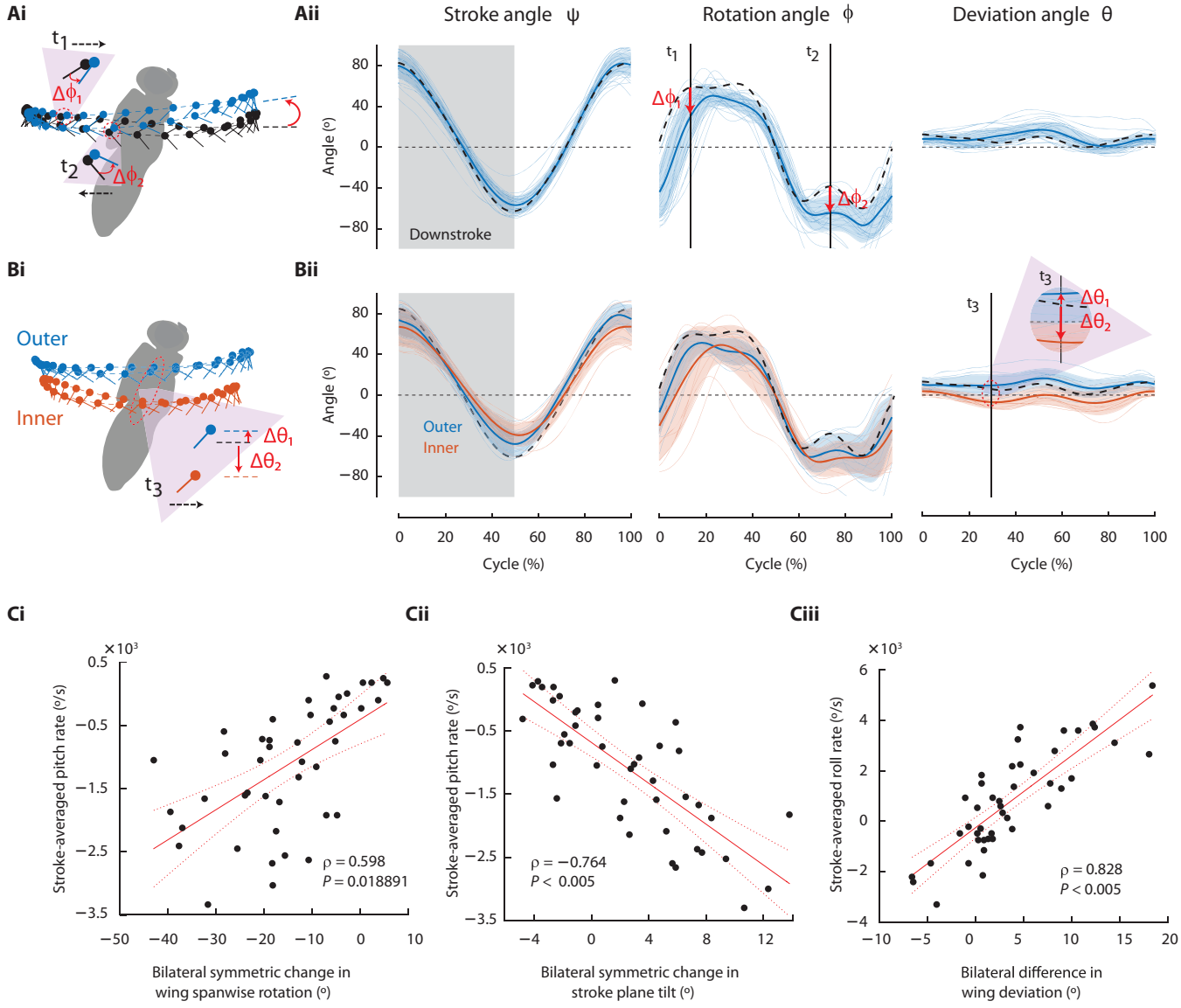

Fig. 5. The rotational maneuvers are generated by the modulation of wing kinematic patterns. (**Ai**) To generate nose-up pitch rotation, a fly tilts its stroke plane backward and shifts its mean wing spanwise rotation angle backward. (**Bi**) To generate roll rotation, a fly elevates the outer wing and lowers the inner wing, thereby tilting its stroke plane laterally toward the inner wing. Changes in the instantaneous wing kinematic patterns for generating pitch (Aii) and roll (Bii) within a time-normalized wingbeat cycle: stroke ψ, rotation ϕ, and deviation θ angles. The thick and thin solid lines represent the averaged and individual wing kinematics. The shaded areas represent ±1 SD. The dashed black lines represent the reference wing kinematics (see fig. S9). The linear regressions between stroke-averaged pitch/roll rates and the changes of wing kinematics are shown with the Pearson's linear correlation coefficient ρ and *P* value. The stroke-averaged pitch rate is strongly correlated with bilateral symmetric change in stroke plane tilt and wing spanwise rotation. The stroke-averaged roll rate is strongly correlated with bilateral asymmetric change in wing deviation (i.e., the lateral tilt of stroke plane).

changes in stroke plane angle (Fig. 5, A and Cii), which were both strongly correlated with the pitch rate (for example, to produce nose-up pitch, the fly tilted its stroke plane and shifted the mean rotation angle backward). Second are the bilateral differences in wing deviation (Fig. 5, B and Ciii), which were strongly correlated with the roll rate. The bilateral differences in wing deviation, which resulted in the lateral tilt of stroke plane, have also been observed in escape maneuvers in hummingbirds (*27*) and fruit flies (*1*). In addition, bilateral differences in wing stroke amplitude and mean wing rotation were observed and likely contributed to the roll. More details of the variables of wing motion changes and their correlations with body angular rates are provided in table S3. Despite the size and physiological differences, the variables of wing motion changes for generating pitch and roll during the inverted landing in flies closely resemble those of hummingbirds during escape maneuvers (*27*).

DISCUSSION

In summary, our results indicate that flies execute inverted landings by a well-coordinated sequence of behavioral modules (Fig. 6), including rapid rotational maneuvers and leg extension, followed by touchdown and a final leg-assisted body swing that brings all feet into contact with the ceiling. The rotational maneuvers were markedly more complex than previously reported in insects landing on surfaces of various orientations (*8*, *12*, *14*, *19*) in studies that mainly highlighted the importance of visually triggered leg extension or deceleration, rather than the rotational maneuvers, for successful landing.

Our results suggest that inverted landing may involve neural processes that not only compute the RRREV that encodes time-to-collision information but also integrate it with other sensory cues that putatively encode multiaxis body linear translation (Fig. 6). Our analyses of the sensory mediation of rotational maneuver (Fig. 3) are entirely correlational at the current time and, as yet, do not establish a causal relationship between sensory cues and the observed maneuvers. However, they do suggest specific hypotheses about how multiple sensory cues could influence landing behavior and success. These data will guide future experiments with controlled manipulation of selected sensory cues from the landing surface, thereby to develop a more complete predictive model of inverted landing.

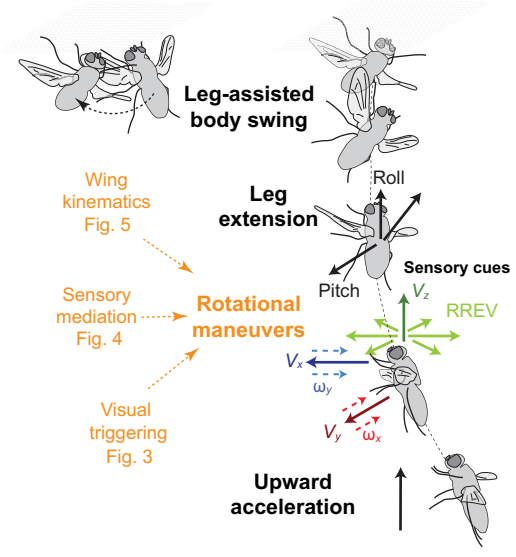

Fig. 6. Summary of visually mediated inverted landing. A fly landing on a ceiling starts with an initial (i) upward acceleration, followed by (ii) rapid rotational maneuvers and (iii) leg extension, and ends with a (iv) leg-assisted body swing with forelegs firmly attached on the ceiling. In successful landing, the rapid rotational maneuvers orient the fly to a proper inversion according its linear velocity. The rotational maneuvers are triggered when RREV exceeds a threshold and are likely mediated by multiple visual (ω_x, ω_y, and RREV) and/or mechanosensory (V_x, V_y, and V_z) cues. The complex behavioral modules observed, particularly the highly variable rotational maneuver, suggest that inverted landing likely involves multiple neural pathways, in addition to those reported earlier for leg extension in vertical landing.

The rotational maneuvers in inverted landing appear to share a similar ballistic nature to the escape responses that initiate the flight (*30*). These maneuvers occurred shortly after startling the flies and immediately before the touchdown and exhibited remarkably high angular velocity. To our knowledge, the values we measured were the maximum reported in actively maneuvering flies. Escape responses in flies are mediated by the giant fiber (GF) that gives rise to fast motor program selection and timing (*30*); the GF also integrates angular expansion velocity and angular size cues and may therefore be responsible for extracting the RREV (*30*). Because both escape and landing are triggered by looming stimuli, it would be important to determine the extent to which these distinct behaviors share common neural pathways.

It can be hypothesized that the variability of the rotational maneuvers arose mainly from the passive flight dynamics in the absence of any sensory mediation, evolving from different initial flight states (*31*, *32*). However, our results do not support this hypothesis. Both computational (*32*, *33*) and experimental (*28*, *34*) results indicate that forward translational velocity induces a pitch-up moment, and the upward translational velocity induces negligible pitch moment in flying insects [see the estimation of stability derivatives (*35*–*39*)]. If the pitch rotation of the flies was mainly determined by the initial flight states via the dynamic processes, this would suggest a negative correlation between the upward velocity and pitch rate and weak correlation between the upward velocity and pitch rate, which contradict the above correlations (Fig. 4Aiii). Thus, we conclude that the correlations between the sensory cues that encoded body linear motion with the roll and pitch rates must result from sensorimotor processes, rather than the passive flight dynamics depending solely on the initial conditions.

In addition to the rotational maneuvers, leg-assisted body swings also exhibited considerable variability in its degree of excursion and the number and types of legs involved. The triggering of leg extension was consistently observed in all successful landings, the timing of which, however, did not follow the onset of rotational maneuvers (Fig. 2, D to F), which were almost absent in landings dominated by leg-assisted body swings (Fig. 2F). Whereas this suggests possible separate neural pathways for leg extension and rotational maneuvers, previous efforts on the neural circuits of landing focused primarily on how leg extension reflex is triggered (*13*, *40*, *41*). The use of legs also appeared to be multifunctional: They can be mainly used to absorb shock (or as a passive braking mechanism) with relatively small body swing (movie S1) or to assist the body swing with large rotation between legs and the body (movie S3). These results are consistent with other observations in houseflies that the leg extension response can be highly variable and depends on local cues such as surface orientation, whereas body deceleration occurs in a more stereotypic fashion (*9*). A recent study also shows that amplitude of the leg extension in *Drosophila* is correlated with the spike rate of two identified descending neuron types, suggesting more finely controlled landing responses (*42*). These observations suggest

that landing behaviors can be thought of as behavioral modules that are either reflexive and rigid or sensory driven and variable (*9*). Therefore, future efforts should focus on identifying the diverse neural mechanisms that trigger and mediate different behavioral modules for the fuller understanding of the neural control of landing.

In addition, because the wings continued to beat during the leg-assisted body swings and showed considerable kinematic changes compared with those prior to touchdown (e.g., movie S3), there was also likely an active, sensory-driven torque generation from the wings. The various aspects of the leg-assisted body swing, including leg extension kinematics, feet contact mechanics, and the aerodynamic forces/torque generation from the wings, should be analyzed in future studies.

Last, our results also suggested that, for small biological or robotic fliers with limited onboard sensing and computing capacity, orchestrating a successful landing hinges critically on the integration of computational (e.g., fast image processing algorithms and circuits) and mechanical (e.g., compliant landing gears or legs) processes. The key visual cues identified in this study can all be estimated from optic flow measurements with relatively low computation (*43*, *44*). They help to trigger and control both the body rotation and the leg extension; body rotation can ensure a proper inversion, where leg extension helps passively damp out the collision and assist in momentum transfer. Recent advances in codesigning algorithms and hardware may offer practical solutions for rapidly computing visual cues on miniature integrated circuit (*45*, *46*), and embedding soft materials into rigid ones can potentially generate compliant landing gears with programmable motions (*47*–*49*).

MATERIALS AND METHODS

Experimental setup and kinematic calculation

Using three high-speed cameras, we captured the behaviors of blue bottle flies (*C. vomitoria*) landing upside down on the ceiling in a flight chamber (Fig. 1A) at the end of flight bouts that were triggered by mechanical vibrations of the chamber. The ceiling, backlit by a light-emitting diode light, was covered by two types of mesh pattern to provide low- or high-visual contrasts. The kinematics of both flies' body and wings were extracted through digitization of anatomical landmarks (Fig. 1B), from which the wing and body principal axes and the corresponding kinematic angles, linear and angular velocities, were calculated (Fig. 1C) (*11*). More details on the experimental setup and kinematic extraction are given in the Supplementary Materials.

Definition of DoI

Here, we defined the DoI of a fly's body orientation shortly before the feet touchdown. Using equation S5 in the Supplementary Materials, we first calculated the magnitude of the geodesic $d_{\Delta R}^{\min}$ (i.e., the shortest distance or the smallest angle) (*50*) between two body orientations: (i) the fly's orientation one wingbeat before the touchdown and (ii) the fully inverted landing orientation. $d_{\Delta R}^{\min}$ ranged from π (having no inversion; i.e., ventral side down) to 0 (being completely inverted; i.e., ventral side up). The DoI was then defined as

$$\mathrm{DoI} = \frac{\pi - d_{\Delta R}^{\min}}{\pi} \quad (1)$$

where DoI = 1 when the fly is completely inverted (i.e., ventral side up), and DoI = 1 when there is no body inversion (i.e., ventral side down).

Calculation of visual cues from body kinematics

The time traces of three putative visual cues were estimated to identify the triggering and visual mediation mechanisms of the rotational maneuvers. The visual cues included the RREV, the relative ceiling fore/aft rotation (ω_y), and the relative ceiling lateral rotation (ω_x). These visual cues can be perceived by a fly from the image sequence projected on its retina without the direct perceptions of the distance or the body velocities. The time traces of these visual cues during the course of inverted landing can be estimated from the measured body kinematics. More details on the kinematic relationships between the visual cues and the body kinematics are given in the Supplementary Materials.

Visual cues in triggering the rotational maneuvers

To analyze how the rotational maneuvers in inverted landings are visually triggered, we calculated the time traces of the CV of three putative visual cues (RREV, ω_y, and ω_x) prior to landing. The CV is a measurement of the dispersion of a variable defined by the ratio of its SD and mean. Assuming that rotational maneuvers are triggered after some time delay when the triggering visual cue reached a threshold at a particular time instant, then the CV of this visual cue at this time instant should be lower than those at other time instants; in addition, the CV of the triggering visual should be lower than those of other nontriggering visual cues. In short, the CV of the triggering visual cue should reach a minimum prior to the triggering moment and be the lowest when compared with the CV of other nontriggering visual cues.

In this analysis, we investigated the triggering of pitch and roll separately. Take the pitch triggering as an example. First, the time traces of the visual cues from different landing trials were aligned at the instant of the start of the pitch. Next, the CV was calculated for each of the visual cues. To identify the triggering visual cue, we first defined a low-value region for the CV of each visual cue (between the two breakpoints that sandwich the low-value valley region of a CV curve), and the visual cue with the lowest minimal CV was identified as the triggering cue. The mean value of this visual cue over the minimum CV range was identified as the triggering threshold. In addition, the time delay in the triggering process due to the sensorimotor transduction can be also identified. Identifying the triggering mechanism for the roll was similar to those for the pitch, except that the time traces of the visual cues were now aligned at the instant of the start of roll.

Sensory cues in mediating the rotational maneuvers

To study whether and how the patterns of rotational maneuvers were mediated by sensory cues in a feedforward fashion after being triggered, we calculated the Pearson's linear correlations between the rotational kinematic features and the putative sensory cues that flies may receive at different time instants prior to or during the rotational maneuvers. The rotational kinematic features tested included the peak, average, and integral of the angular velocities (p, q, and r) of the rotational maneuvers. The putative sensory cues tested included the visual (RREV, ω_x, and ω_y) and mechanosensory cues (V_x, V_y, and V_z). After some preliminary testing and analysis, it was determined that the peak pitch and roll rates best represent the patterns of rotational maneuvers as they also had the strongest correlations with the sensory cues compared with other rotational kinematic features. Therefore, next we calculated the time traces of the correlations between the peak angular rates and the sensory cues at different time instants prior to the moment of peak angular rates. For example, to calculate the correlation between the peak pitch rate and the RREV, the time traces of the RREV from different landing trials were first aligned at the instant of peak pitch rate; then,

the time trace of the Pearson's linear correlations between the peak pitch rate and the RREV at varying time instants prior to the peak pitch rate was calculated.

Wing kinematics in generating rotational maneuvers

The recorded wing kinematics were represented by the stroke ψ, deviation θ, and rotation ϕ angles and parameterized using Fourier series. These wingbeats were classified into reference and pitch- or roll-generating ones based on their corresponding angular accelerations. More details are given in the Supplementary Materials. To investigate the changes of wing motion that produced the rotational maneuvers, the Pearson's linear correlations between the changes of wing kinematic variables and body angular velocity and accelerations were calculated. The changes of wing kinematic variables include bilateral symmetric and asymmetric changes of stroke angle, wing rotation and deviation, stroke plane tilt, and wingbeat frequency. In addition, the correlation with stroke-averaged upward acceleration was also calculated.

SUPPLEMENTARY MATERIALS

Supplementary material for this article is available at http://advances.sciencemag.org/cgi/content/full/5/10/eaax1877/DC1

Supplementary Materials and Methods

Fig. S1. Relationship between the visual cues and the fly's body translational kinematics.

Fig. S2. Sketches of flight sequences of two failed landing attempts and the corresponding kinematics.

Fig. S3. Time traces of body kinematics of landing maneuvers dominated by pitch and roll.

Fig. S4. The pitch rotation in inverted landings is triggered when RREV exceeds a threshold.

Fig. S5. The roll rotation in inverted landings is triggered when RREV exceeds a threshold.

Fig. S6. Correlations between visual or mechanosensory cues to the pitch rate of the rotational maneuvers.

Fig. S7. Correlations between visual or mechanosensory cues to the roll rate of the rotational maneuvers.

Fig. S8. Linear regressions between peak pitch (or roll) rate and sensory cues at an example time instant of 20 ms before the time instant of the peak pitch (or roll) rate.

Fig. S9. The wing kinematics that generate upward acceleration prior to rotational maneuvers are defined as the reference wing kinematics.

Table S1. Categorized landing trials.

Table S2. The Pearson's linear correlation coefficient and *P* value between body rotation variables and multiple sensory cues at an example time instant of 20 ms before peak of rotation rate.

Table S3. The Pearson's linear correlation coefficient and *P* value between body kinematic variables and the changes of wing kinematic variables.

Movie S1. High-speed video recordings of an example pitch-dominated landing (PD) shown in Fig. 1D.

Movie S2. High-speed video recordings of an example roll-dominated landing (RD) shown in Fig. 1E.

Movie S3. High-speed video recordings of an example longitudinal-body-swing-dominated landing (SLon) shown in Fig. 1F.

Movie S4. High-speed video recordings of an example lateral-body-swing-dominated landing (SLat).

Movie S5. High-speed video recordings of an example pitch-roll combined landing (PR).

Movie S6. High-speed video recordings of an example landing with ceiling groping (CG).

Movie S7. High-speed video recordings of an example failed landing due to early body rotation (FER) shown in Fig. S2A.

Movie S8. High-speed video recordings of an example failed landing due to low body inversion with delayed leg extension (FDE) shown in Fig. S2B.

Movie S9. High-speed video recordings of an example failed landing due to low body inversion with minor body rotation (FMR).

References (*51*, *52*)

View/request a protocol for this paper from *Bio-protocol*.

REFERENCES AND NOTES

1. F. T. Muijres, M. J. Elzinga, J. M. Melis, M. H. Dickinson, Flies evade looming targets by executing rapid visually directed banked turns. *Science* **344**, 172–177 (2014).
2. T. Beatus, J. M. Guckenheimer, I. Cohen, Controlling roll perturbations in fruit flies. *J. R. Soc. Interface* **12**, 20150075 (2015).
3. R. C. Wilkerson, J. F. Butler, The Immelmann Turn, a pursuit maneuver used by hovering male Hybomitra hinei wrighti (Diptera: Tabanidae). *Ann. Entomol. Soc. Am.* **77**, 293–295 (1984).
4. W. G. Hyzer, Flight behavior of a fly alighting on a ceiling. *Science* **137**, 609–610 (1962).
5. M. Kovac, Learning from nature how to land aerial robots. *Science* **352**, 895–896 (2016).
6. K. Jayaram, J.-M. Mongeau, A. Mohapatra, P. Birkmeyer, R. S. Fearing, R. J. Full, Transition by head-on collision: Mechanically mediated manoeuvres in cockroaches and small robots. *J. R. Soc. Interface* **15**, 20170664 (2018).
7. C. Shen, M. Sun, Wing and body kinematics measurement and force analyses of landing in fruit flies. *Bioinspir. Biomim.* **13**, 016004 (2018).
8. F. Van Breugel, M. H. Dickinson, The visual control of landing and obstacle avoidance in the fruit fly Drosophila melanogaster. *J. Exp. Biol.* **215**, 1783–1798 (2012).
9. S. P. Sane, S. Balebail, S. K. Raja, Visual control of landing maneuvers in houseflies on vertical and inverted surfaces. *bioRxiv* 10.1101/448472 (2018).
10. S. Dalton, J. Kings, *Borne On The Wind: The Extraordinary World Of Insects In Flight* (1975).
11. S. N. Gorb, Uncovering insect stickiness: Structure and properties of hairy attachment devices. *Am. Entomologist* **51**, 31–35 (2005).
12. A. Borst, How do flies land? *Bioscience* **40**, 292–299 (1990).
13. A. Borst, Time course of the houseflies' landing response. *Biol. Cybern.* **54**, 379–383 (1986).
14. H. Wagner, Flow-field variables trigger landing in flies. *Nature* **297**, 147–148 (1982).
15. B. Cheng, B. W. Tobalske, D. R. Powers, T. L. Hedrick, Y. Wang, S. M. Wethington, G. T.-C. Chiu, X. Deng, Flight mechanics and control of escape manoeuvres in hummingbirds. II. Aerodynamic force production, flight control and performance limitations. *J. Exp. Biol.* **219**, 3532–3543 (2016).
16. W. R. Roderick, M. R. Cutkosky, D. Lentink, Touchdown to take-off: At the interface of flight and surface locomotion. *Interface Focus* **7**, 20160094 (2017).
17. M. V. Srinivasan, S.-W. Zhang, J. S. Chahl, E. Barth, S. Venkatesh, How honeybees make grazing landings on flat surfaces. *Biol. Cybern.* **83**, 171–183 (2000).
18. D. N. Lee, A theory of visual control of braking based on information about time-to-collision. *Perception* **5**, 437–459 (1976).
19. E. Baird, N. Boeddeker, M. R. Ibbotson, M. V. Srinivasan, A universal strategy for visually guided landing. *Proc. Natl. Acad. Sci.* **110**, 18686–18691 (2013).
20. M. Srinivasan, How insects infer range from visual motion. *Rev. Oculomot. Res.* **5**, 139 (1993).
21. T. Collett, Depth vision in animals. *Analysis of visual behavior* 111–176 (1982).
22. S. B. Fuller, A. D. Straw, M. Y. Peek, R. M. Murray, M. H. Dickinson, Flying Drosophila stabilize their vision-based velocity controller by sensing wind with their antennae. *Proc. Natl. Acad. Sci.* **111**, E1182–E1191 (2014).
23. J.-M. Mongeau, M. A. Frye, Drosophila spatiotemporally integrates visual signals to control saccades. *Curr. Biol.* **27**, 2901–2914. e2 (2017).
24. J. C. Theobald, D. L. Ringach, M. A. Frye, Dynamics of optomotor responses in Drosophila to perturbations in optic flow. *J. Exp. Biol.* **213**, 1366–1375 (2010).
25. T. Lindsay, A. Sustar, M. Dickinson, The function and organization of the motor system controlling flight maneuvers in flies. *Curr. Biol.* **27**, 345–358 (2017).
26. M. H. Dickinson, The initiation and control of rapid flight maneuvers in fruit flies. *Integr. Comp. Biol.* **45**, 274–281 (2005).
27. B. Cheng, B. W. Tobalske, D. R. Powers, T. L. Hedrick, S. M. Wethington, G. T. Chiu, X. Deng, Flight mechanics and control of escape manoeuvres in hummingbirds. I. Flight kinematics. *J. Exp. Biol.* **219**, 3518–3531 (2016).
28. B. Cheng, X. Deng, T. L. Hedrick, The mechanics and control of pitching manoeuvres in a freely flying hawkmoth (Manduca sexta). *J. Exp. Biol.* **214**, 4092–4106 (2011).
29. G. K. Taylor, H. G. Krapp, S. J. Simpson, Sensory systems and flight stability: What do insects measure and why? *Adv. In Insect Phys.* **34**, 231–316 (2007).
30. C. R. von Reyn, A. Nern, W. R. Williamson, P. Breads, M. Wu, S. Namiki, G. M. Card, Feature integration drives probabilistic behavior in the Drosophila escape response. *Neuron* **94**, 1190–1204.e6 (2017).
31. M. Sun, Insect flight dynamics: Stability and control. *Rev. Mod. Phys.* **86**, 615–646 (2014).
32. B. Liang, M. Sun, Nonlinear flight dynamics and stability of hovering model insects. *J. R. Soc. Interface* **10**, 20130269 (2013).
33. Y. Xiong, M. Sun, Dynamic flight stability of a bumblebee in forward flight. *Acta Mech. Sin.* **24**, 25–36 (2008).
34. M. J. Elzinga, F. van Breugel, M. H. Dickinson, Strategies for the stabilization of longitudinal forward flapping flight revealed using a dynamically-scaled robotic fly. *Bioinspir. Biomim.* **9**, 025001 (2014).
35. M. Sun, Y. Xiong, Dynamic flight stability of a hovering bumblebee. *J. Exp. Biol.* **208**, 447–459 (2005).
36. L. Ristroph, G. Ristroph, S. Morozova, A. J. Bergou, S. Chang, J. Guckenheimer, Z. J. Wang, I. Cohen, Active and passive stabilization of body pitch in insect flight. *J. R. Soc. Interface* **10**, 20130237 (2013).

37. I. Faruque, J. Sean Humbert, Dipteran insect flight dynamics. Part 1 Longitudinal motion about hover. *J. Theor. Biol.* **264**, 538–552 (2010).
38. B. Cheng, X. Deng, Translational and rotational damping of flapping flight and its dynamics and stability at hovering. *IEEE Trans. Robot.* **27**, 849–864 (2011).
39. M. Sun, J. K. Wang, Flight stabilization control of a hovering model insect. *J. Exp. Biol.* **210**, 2714–2722 (2007).
40. A. Borst, S. Bahde, What kind of movement detector is triggering the landing response of the housefly? *Biol. Cybern.* **55**, 59–69 (1986).
41. H. Eckert, K. Hamdorf, Excitatory and inhibitory response components in the landing response of the blowfly, Calliphora erythrocephala. *J. Comp. Physiol.* **138**, 253–264 (1980).
42. J. M. Ache, S. Namiki, A. Lee, K. Branson, G. M. Card, State-dependent decoupling of sensory and motor circuits underlies behavioral flexibility in Drosophila. *Nat. Neurosci.* **22**, 1132–1139 (2019).
43. E. Ilg, N. Mayer, T. Saikia, M. Keuper, A. Dosovitskiy, T. Brox, Flownet 2.0: Evolution of optical flow estimation with deep networks, in *Proceedings of the IEEE Conference on Computer Vision and Pattern Recognition* (2017), pp 2462–2470.
44. T. Kroeger, R. Timofte, D. Dai, L. Van Gool, Fast optical flow using dense inverse search, in *European Conference on Computer Vision* (Springer, 2016), pp 471–488.
45. L. Carlone, S. Karaman, Attention and anticipation in fast visual-inertial navigation. *IEEE Trans. Robot.* **35**, 1–20 (2019).
46. A. Suleiman, Z. Zhang, L. Carlone, S. Karaman, V. Sze, Navion: A 2-mW fully integrated real-time visual-inertial odometry accelerator for autonomous navigation of nano drones. *IEEE J. Solid-State Circuits* **54**, 1106–1119 (2019).
47. J. A. Faber, A. F. Arrieta, A. R. Studart, Bioinspired spring origami. *Science* **359**, 1386–1391 (2018).
48. C. Coulais, A. Sabbadini, F. Vink, M. van Hecke, Multi-step self-guided pathways for shape-changing metamaterials. *Nature* **561**, 512–515 (2018).
49. M. Stern, V. Jayaram, A. Murugan, Shaping the topology of folding pathways in mechanical systems. *Nat. Commun.* **9**, 4303 (2018).
50. J. M. Lee, *Riemannian manifolds: An introduction to curvature* (Springer Science & Business Media, 2006).
51. T. L. Hedrick, Software techniques for two- and three-dimensional kinematic measurements of biological and biomimetic systems. *Bioinspir. Biomim.* **3**, 034001 (2008).
52. R. M. Murray, Z. Li, S. S. Sastry, *A Mathematical Introduction to Robotic Manipulation* (CRC, 1994).

Acknowledgments: We thank X. Wang and D. Yeung for assistance with the high-speed video recordings, digitizing landing kinematics, and data analyses. **Funding:** This research was supported by the National Science Foundation (CMMI-1554429 and IIS-1815519 to B.C. and IIS-1815476 to J.Z.) and the Pennsylvania State University. **Author contributions:** P.L., B.C., and S.P.S. contributed to the design of the experiments; P.L. and B.C. performed the experiments; P.L. analyzed the data; P.L., B.C., S.P.S., J.-M.M., and J.Z. contributed to the interpretation of findings and the preparation of the manuscript. **Competing interests:** The authors declare that they have no financial or other competing interests. **Data and materials availability:** All data needed to evaluate the conclusions in the paper are present in the paper and/or the Supplementary Materials. Additional data related to this paper may be requested from the authors.

Submitted 28 February 2019
Accepted 14 September 2019
Published 23 October 2019
10.1126/sciadv.aax1877

Citation: P. Liu, S. P. Sane, J.-M. Mongeau, J. Zhao, B. Cheng, Flies land upside down on a ceiling using rapid visually mediated rotational maneuvers. *Sci. Adv.* **5**, eaax1877 (2019).

Flies land upside down on a ceiling using rapid visually mediated rotational maneuvers

Pan Liu, Sanjay P. Sane, Jean-Michel Mongeau, Jianguo Zhao and Bo Cheng

Sci Adv **5** (10), eaax1877.
DOI: 10.1126/sciadv.aax1877

Science Advances
AAAS

advances.sciencemag.org/cgi/content/full/5/10/eaax1877/DC1

Supplementary Materials for

Flies land upside down on a ceiling using rapid visually mediated rotational maneuvers

Pan Liu, Sanjay P. Sane, Jean-Michel Mongeau, Jianguo Zhao, Bo Cheng*

*Corresponding author. Email: buc10@psu.edu

Published 23 October 2019, *Sci. Adv.* **5**, eaax1877 (2019)
DOI: 10.1126/sciadv.aax1877

The PDF file includes:

Other Supplementary Material for this manuscript includes the following:

(available at advances.sciencemag.org/cgi/content/full/5/10/eaax1877/DC1)

Table S3 (Microsoft Excel format). The Pearson's linear correlation coefficient and *P* value between body kinematic variables and the changes of wing kinematic variables.
Movie S1 (.mp4 format). High-speed video recordings of an example pitch-dominated landing (PD) shown in Fig. 1D.
Movie S2 (.mp4 format). High-speed video recordings of an example roll-dominated landing (RD) shown in Fig. 1E.
Movie S3 (.mp4 format). High-speed video recordings of an example longitudinal-body-swing-dominated landing (SLon) shown in Fig. 1F.
Movie S4 (.mp4 format). High-speed video recordings of an example lateral-body-swing-dominated landing (SLat).
Movie S5 (.mp4 format). High-speed video recordings of an example pitch-roll combined landing (PR).
Movie S6 (.mp4 format). High-speed video recordings of an example landing with ceiling groping (CG).
Movie S7 (.mp4 format). High-speed video recordings of an example failed landing due to early body rotation (FER) shown in fig. S2A.
Movie S8 (.mp4 format). High-speed video recordings of an example failed landing due to low body inversion with delayed leg extension (FDE) shown in fig. S2B.
Movie S9 (.mp4 format). High-speed video recordings of an example failed landing due to low body inversion with minor body rotation (FMR).

Supplementary Materials and Methods

Experimental setup

The experimental setup mainly consisted of a flight chamber (20cm × 20cm × 20cm), three high-speed cameras, and LED light sources (Fig. 1A). The flight chamber was made of a transparent acrylic box with a 10 cm × 10 cm landing area on the center of its ceiling that was cut open. The landing area was made of a layer of fabric mesh (on the top) to enhance the visual contrast, and a layer of transparent plastic film (on the bottom), on which the flies would land. The mesh and film were stretched so that they remained approximately rigid (with negligible deformation) when flies landed. Two types of mesh patterns, one in white with an average grid size of 15 mm^2 and one in black with an average grid size of 0.94 mm^2, were used in the experiments to provide different visual contrasts when flies landed.

Experiments were performed using 3-7 days old blue bottle flies (*Calliphora vomitoria*) (29 ± 4 mg) hatched from pupae (Mantisplace, Olmsted Twp., OH, USA). After being cold-anesthetized for 10 minutes, the flies were introduced to the flight chamber in a group of 20 to 30 for each experiment. The experiments were performed in the flight chamber after flies fully recovered from the cold-anesthetization. During each experiment, the experimenter introduced mechanical vibration to the chamber as the stimulus eliciting flight bouts of the flies, which ended with landing on one of the chamber's surfaces.

We recorded the landing trials within the landing area using three synchronized high-speed cameras (FASTCAM Mini UX100, Photron Inc., San Diego, CA, USA), operating at 5,000 frames/s with exposure of 1/25,600 s. The cameras were calibrated using a direct linear transformation for three-dimensional kinematic reconstruction (51) before and after each experiment. During the experiments, the high-speed cameras were manually triggered when attempts of landing (including successful, failed and groping) on the landing area were observed. The flies and the landing area were backlit in the cameras by three 50-W LED light sources (MonoBright LED750, Genaray Co., Brooklyn, NY, USA), placed outside the flight chamber (Fig 1A). A thin diffusing filter was placed in front of each LED light to generate more homogeneous light filed. The anatomical landmarks on the body and wings of the flies (Fig. 1B) in the captured images were then digitized in MATLAB (MathWorks, Natick, MA, USA) using DLTdv6 (51).

Analysis of body kinematics

Body translational and rotational kinematics, including position, linear velocity, three Euler angles that parameterize body orientation (i.e. roll, pitch and yaw angles), and angular velocity (i.e. roll, pitch and yaw rate), were directly calculated from the four digitized points on the body (1 to 4 in Fig. 1A). In this process, three reference frames were defined, i.e. the global frame of reference $\mathcal{F}_g = \{x_g, y_g, z_g\}$ with z_g-axis pointing vertically upwards and x_g-y_g on the horizontal plane; the body-fixed frame of reference $\mathcal{F}_b = \{x_b, y_b, z_b\}$ (Fig. 1C) with x_b from rear end of abdomen to head, y_b from right wing base to left wing base and z_b being the cross product of the two; and the yaw-aligned global frame $\mathcal{F} = \{x, y, z\}$ (Fig. 1C) obtained via rotating the frame $\mathcal{F}_g$ about the z_g axis by the fly's yaw angle.

The body position, $\boldsymbol{p}_b$, was determined by the location of the centroid of the four digitized points on body (1 to 4 in Fig. 1A), i.e.

$$\boldsymbol{p}_b = \frac{1}{n}\sum_{i=1}^{n=4} \boldsymbol{p}_i \tag{1}$$

where $\boldsymbol{p}_i$ is the position vector of the i-th digitized point. The body translational velocity was expressed in different frames, i.e. $\boldsymbol{v}_b^{\mathcal{F}_g}$, $\boldsymbol{v}_b^{\mathcal{F}_b}$ and $\boldsymbol{v}_b^{\mathcal{F}}$, and was obtained by differentiating $\boldsymbol{p}_b$ followed by rotations to the corresponding reference frame, for example

$$\boldsymbol{v}_b^{\mathcal{F}_b} = \boldsymbol{R}_g^b * \boldsymbol{v}_b^{\mathcal{F}_g} = \boldsymbol{R}_g^b * \frac{d}{dt}\,\boldsymbol{p}_b \tag{2}$$

where t is time and the rotation matrix from $\mathcal{F}_g$ to $\mathcal{F}_b$ is denoted by $\boldsymbol{R}_g^b$, whose transpose is formed in columns by the body-fixed frame axes, i.e.

$$\left(\boldsymbol{R}_g^b\right)^T = \boldsymbol{R}_b^g = [x_b, y_b, z_b] \tag{3}$$

The rotation matrix $\boldsymbol{R}_b^g$ is an unique representation of the body orientation , from which the body roll ϕ_b, pitch θ_b and yaw ψ_b angles (in the sequence of Z-Y-X), as well as the roll p, pitch q and yaw r rate were calculated (52).

Distance travelled by the fly's rotational trajectory

The total distance travelled by a fly's translational trajectory was approximated by the summation of the distance between two consecutive body positions. The total distance travelled by a fly's rotational trajectory $\boldsymbol{R}(t)$ (the time traces of the body orientation), $d_{\boldsymbol{R}(t)}$, was estimated according to

$$d_{\boldsymbol{R}(t)} = \sum_{i=1}^{N} d[\boldsymbol{R}(t_i), \boldsymbol{R}(t_{i+1})] \tag{4}$$

where $d[\boldsymbol{R}(t_i), \boldsymbol{R}(t_{i+1})]$ is the distance between two consecutive body orientations $\boldsymbol{R}(t_i)$ and $\boldsymbol{R}(t_{i+1})$, referred to as the (magnitude of) geodesic (50). When a proper bi-invariant metric is selected to define the distance in the special orthogonal group $SO(3)$(i.e., the configuration space of all rigid body orientations), $d[\boldsymbol{R}(t_i), \boldsymbol{R}(t_{i+1})]$ is equivalent to the angle of the non-unity eigenvalue λ (generally a complex number) of the matrix $\boldsymbol{R}(t_i)^{-1} * \boldsymbol{R}(t_{i+1})$

$$d[\boldsymbol{R}(t_i), \boldsymbol{R}(t_{i+1})] = |\arg(\lambda)|, \text{where } \lambda \neq 1 \tag{5}$$

In our analysis, we used Eqn. S4 to calculate the $d_{\boldsymbol{R}(t)}$ according to the trajectories of the rotational maneuvers from the start of rotation to the moment of feet touchdown (fig. S3vi).

We also used Eqn. S5 to calculate the magnitude of geodesic $d_{\Delta R}^{\min}$ (i.e., the shortest distance or the smallest angle) between two body orientations: the fly's orientation one-wingbeat before the feet touchdown and the ideal inverted landing orientation. $d_{\Delta R}^{\min}$ was used in the calculation of Degree of Inversion (DoI) in the Materials and Methods.

Calculation of visual cues from body kinematics

Here the kinematic relationships between the visual cues and the body kinematics are established. The visual cues include Relative Retinal Expansion Velocity (RREV), relative ceiling fore/aft rotation (ω_y) and relative ceiling lateral rotation (ω_x), which result from vertical velocity V_z, forward/backward velocity V_x and lateral velocity V_y, respectively (fig S1).

RREV results from looming stimuli as a fly approaches ceiling (fig. S1A), and is the reciprocal of time-to-collision. As derived below, RREV can be extracted directly from visual information without the explicit knowledge of distance to the ceiling or the upward velocity. Considering a fly approaches ceiling with a distance z and an upward velocity V_z, a feature point on the ceiling that is distance r from the fly's approaching point has a viewing angle γ (fig. S1A)

$$\tan\gamma = \frac{r}{z} \tag{6}$$

Taking the time derivative of both sides (here r is considered as constant) yields

$$\frac{1}{\cos^2\gamma}\frac{d\gamma}{dt} = -\frac{r}{z^2}\frac{dz}{dt} \tag{7}$$

Since $\frac{r}{z} = \tan\gamma$ and $\frac{dz}{dt} = V_z$, we have

$$\frac{2}{\sin 2\gamma}\frac{d\gamma}{dt} = -\frac{V_z}{z} = -\text{RREV} \tag{8}$$

This indicates that the RREV, which equals to $\frac{V_z}{z}$ (the reciprocal of time-to-collision), can be extracted from (1) $\frac{d\gamma}{dt}$ (retinal expansion velocity of the feature point) and (2) $\frac{\sin 2\gamma}{2} \approx \gamma$ (when γ is small), which is related to the viewing angle or the retinal size of the feature point. Both quantities represent visual information that can be obtained from the retinal motion image. The $\frac{d\gamma}{dt}$ encodes the radial expansion rate of the feature point and γ encodes the radial distance of the feature point.

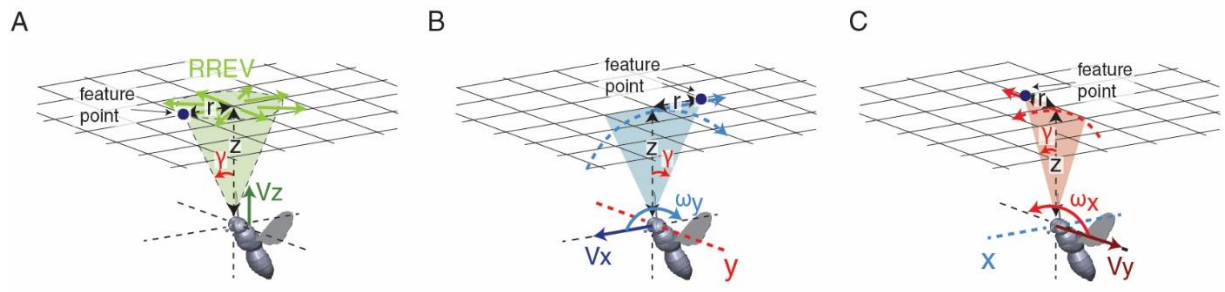

Fig. S1. Relationship between the visual cues and the fly's body translational kinematics. (**A**) When approaching the ceiling with an upward velocity V_z, a fly can perceive Relative Retinal

Expansion Velocity (RREV) of the ceiling on its retina. (**B**) When flying forward with a velocity V_x, the ceiling rotates backwards about the y axis on fly's retina, the angular velocity of which is defined as ω_y. (**C**) Similarly, a lateral velocity of the fly V_y results in a lateral rotation of the ceiling about x axis on the retina (ω_x). The z is the distance of the fly from the ceiling, r is the radius of a feature point on the ceiling from the approaching point, and γ is the viewing angle of the feature point. The visual cues: RREV, ω_y and ω_x, are the results of linear velocities V_z, V_x and V_y, respectively, and can be calculated from the visual information derived from viewing angle γ and its expansion rate $\frac{d\gamma}{dt}$, without explicitly knowing the distance z or the body linear velocities (20, 21).

In addition, one can calculate the fore/aft angular velocity of the ceiling, perceived by the flow field on the fly's retina (ω_y, fig. S1 B). Considering a fly flying forward under the ceiling with a vertical distance z towards to ceiling and a forward velocity V_x (fig. S1 B), a feature point on the ceiling that is distance r from the center in fore/aft direction has a viewing angle γ

$$\tan\gamma = \frac{r}{z} \tag{9}$$

Taking the time derivative of both sides (here z is considered as constant) yields

$$\frac{1}{\cos^2\gamma}\frac{d\gamma}{dt} = \frac{1}{z}\frac{dr}{dt} \tag{10}$$

Since $\frac{dr}{dt} = V_x$, we have

$$\frac{2}{1+\cos 2\gamma}\frac{d\gamma}{dt} = \frac{V_x}{z} = \omega_y \tag{6}$$

This indicates that ω_y, which equals to $\frac{V_x}{z}$, can be extracted from the visual information $\frac{d\gamma}{dt}$ and $\cos 2\gamma$, without the explicit knowledge of V_x or z. The $\frac{d\gamma}{dt}$ encodes the radial expansion rate of the feature point and $\cos 2\gamma$ encodes the distance of the feature point from the center in fore/aft direction.

Similarly, the lateral angular velocity of the ceiling perceived by the flow field on the fly's retina ω_x (fig. S1 C), can be obtained as following

$$\frac{2}{1+\cos 2\gamma}\frac{d\gamma}{dt} = \frac{V_y}{z} = \omega_x \tag{12}$$

Analysis of wing kinematics

The wing kinematics were determined by the coordinate transformations between the wing stroke plane frame $\mathcal{F}_s$ and the wing-fixed frame $\mathcal{F}_w$. The periodic wingbeat patterns and their cycle-wise variations, were represented by Fourier Series. The wingbeat patterns were classified as reference, pitch or roll generating according to the average body roll and pitch accelerations

within an individual wingbeat. The nominal wingbeat pattern of a class was defined as the averaged pattern within the class.

For each wing, a wing-fixed frame of reference $\mathcal{F}_w = \{x_w, y_w, z_w\}$ was defined with y_w along the wing leading edge, z_w aligned with the wing chord perpendicular to the leading edge, and x_w being their cross product. The stroke plane frame $\mathcal{F}_s = \{x_s, y_s, z_s\}$ (fig. S4 Ci) was defined according to the nominal stroke plane, which was assumed to be 45° rotated from the $x_b - y_b$ plane. Therefore, it was obtained via rotating the body reference frame $\mathcal{F}_b$ about y_b axis by 45°. The wing Euler angles, including rotation ϕ, deviation θ and stroke ψ, were obtained from the three consecutive single-axis rotations from $\mathcal{F}_s$ to $\mathcal{F}_w$ in the sequence of ZXY (52). The time series of wing Euler angles were then parameterized using 8th order Fourier series prior to further analysis

$$\begin{aligned}
\phi(\hat{t}) &= \phi_{w0} + \sum_{i=1}^{8} \phi_{w_{si}} \sin 2\pi i\hat{t} + \phi_{w_{ci}} \cos 2\pi i\hat{t} \\
\theta(\hat{t}) &= \theta_{w0} + \sum_{i=1}^{8} \theta_{w_{si}} \sin 2\pi i\hat{t} + \theta_{w_{ci}} \cos 2\pi i\hat{t} \\
\psi(\hat{t}) &= \psi_{w0} + \sum_{i=1}^{8} \psi_{w_{si}} \sin 2\pi i\hat{t} + \psi_{w_{ci}} \cos 2\pi i\hat{t}
\end{aligned} \tag{7}$$

where $\hat{t}$ was normalized time from 0 to 1 for each wingbeat cycle, and ϕ_{w0}, $\phi_{w_{si}}$, $\phi_{w_{ci}}$, etc. were the Fourier series coefficients. Having the Fourier series for all recorded wingbeats, the nominal wingbeat patterns for the classified wingbeats were obtained by averaging the corresponding Fourier series. The classification of wingbeats into reference and pitch or roll-generating wingbeat patterns was based on the thresholds defined as half of the maximum angular acceleration in the corresponding trial. For example, a wingbeat was classified as pitch or roll-generating if its cycle-averaged pitch or roll acceleration exceeded half of the maximum pitch or roll acceleration, respectively. A wingbeat was classified as reference if its cycle-averaged body angular acceleration was lower than the half of the maximum angular acceleration in the corresponding trial of the landing maneuver. The roll or pitch generating wingbeat patterns were then compared with the reference ones to find the changes of wing kinematics during the landing maneuvers.

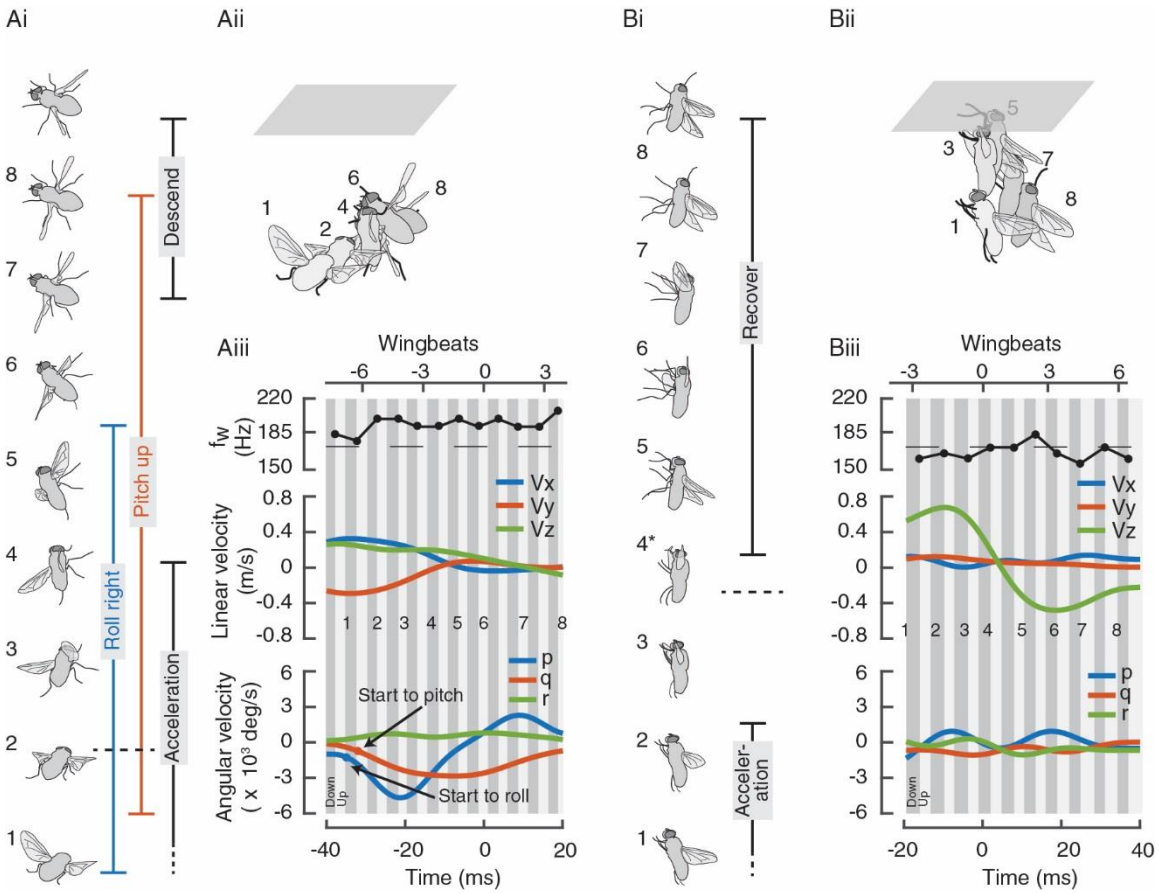

Fig. S2. Sketches of flight sequences of two failed landing attempts and the corresponding kinematics. Failed landing attempts are due to early body rotation (Movie S7), or low body inversion with late body rotation/leg extension (Movie S8). (**A**) Early body rotation without sufficient upward velocity results in a loss of altitude before touching the ceiling. (**B**) On the contrary, delayed leg extension and low body inversion result in an undesired impact angle and leg posture towards the ceiling. Consequently, the fly's feet cannot properly plant on the ceiling, and the upward linear momentum cannot be damped out or being transferred to angular momentum; the fly collides and is then bounced back from the ceiling. The two failed landing attempts underline the importance of proper timings of rotational maneuvers and the coordination of translational and rotational motions. (i) Sketches of flight sequences are separated spatially to make each instance visible. (ii) Sketches of flight sequences are shown in their actual relative spatial locations. (iii) Time traces of the wingbeat frequency f_w, body translational velocities V_x, V_y and V_z, and body rotational velocities p, q and r, similar to those described in Fig. 1 for successful landing cases. Time 0 indicates the moment when a fly reaches the highest altitude (A) or touches the ceiling (B).

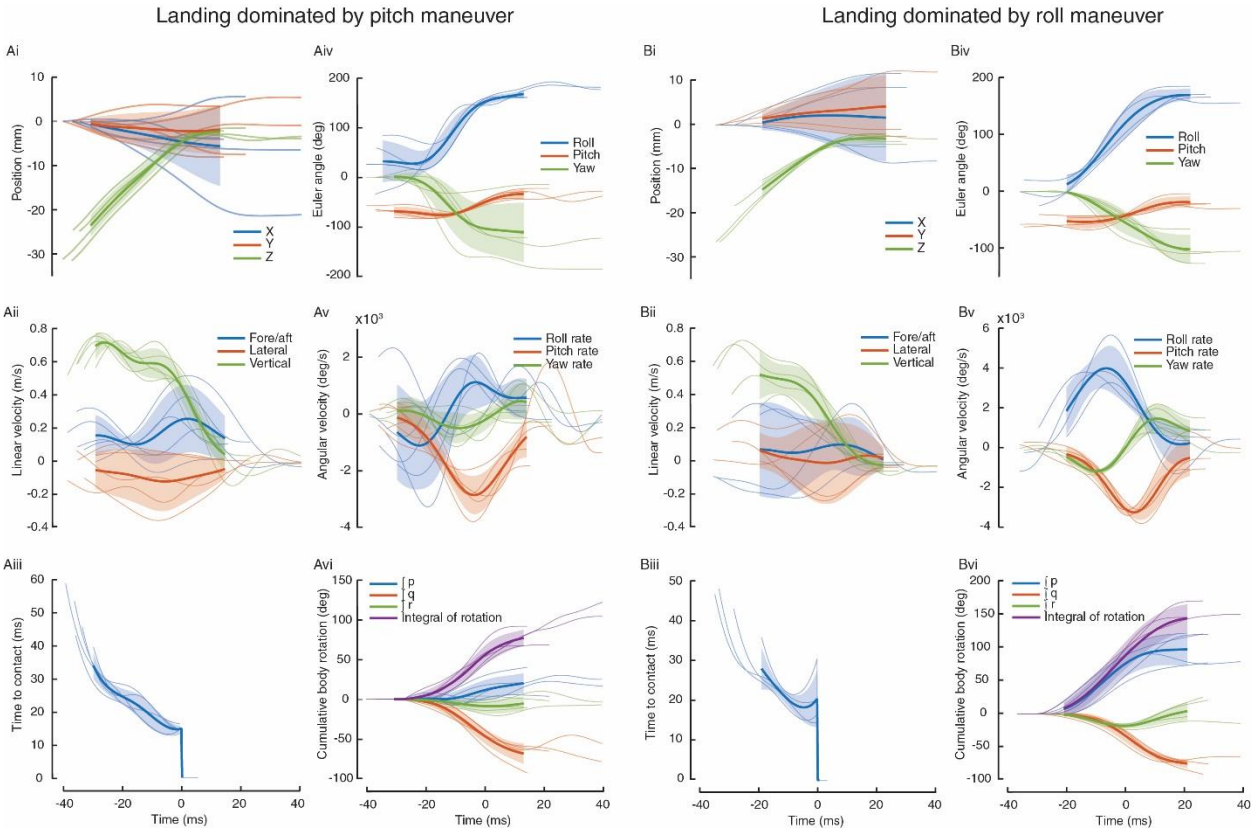

Fig. S3. Time traces of body kinematics of landing maneuvers dominated by pitch and roll. (**A**) landing dominated by pitch rotational maneuver, (**B**) landing dominated by roll rotational maneuver. Kinematic variables include (i) body position, (ii) body translational velocity, (iii) time to collision, (iv) body Euler angles, (v) body angular velocity and (vi) integral of body rotation $d_{\boldsymbol{R}(t)}$, according to Eqn. S4. The time traces of different maneuvers are aligned at the instants when flies' feet first touch ceiling (time 0). The thick and thin lines represent the averaged and individual traces, respectively. The shaded areas indicate ± 1 s.d. During the pitch-dominated landing, a fly ascends upwards with an average body pitch angle approximately 70°, followed by a rapid pitching up, reaching the peak angular velocity within 8 wingbeats (<50 ms) before touchdown, and finally attains a ventral-side-up orientation after an additional leg-assisted body swing. In the meanwhile, there is a small amount of roll motion that orients the fly body towards the resultant velocity of V_x and V_y. On the other hand, in roll-dominated landing, the roll rate peaks within 5 wingbeats and can be as high as 6000 degree/s, steering the body towards a ventral-side-up orientation before touchdown. It is then followed by an additional leg-assisted body swing that brings the body fully ventral-side-up (body longitudinal axis aligns with the ceiling).

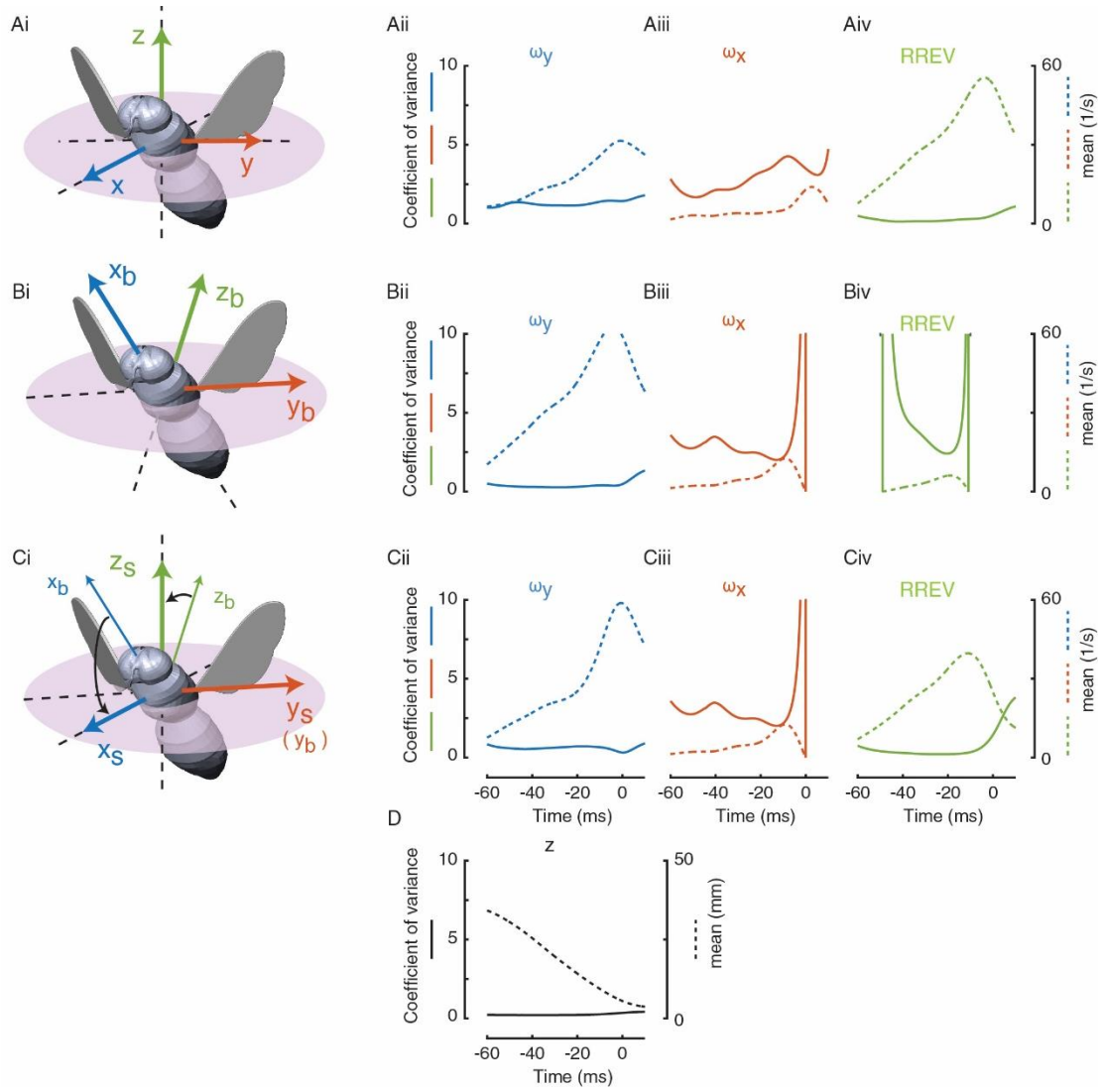

Fig. S4. The pitch rotation in inverted landings is triggered when RREV exceeds a threshold. Time traces of coefficients of variation (c.v.) and mean values of the visual cues are calculated with respect to three sets of coordinate frames: (**A**) yaw-aligned global frame $\mathcal{F} = \{x, y, z\}$, (**B**) body fixed frame $\mathcal{F}_b = \{x_b, y_b, z_b\}$ and (**C**) stroke plane frame $\mathcal{F}_s = \{x_s, y_s, z_s\}$ generated by pitching down $\mathcal{F}_b$ about the y_b axis by 45 degrees. The visual cues include (ii) ω_y, (iii) ω_x and (iv) RREV. (**D**) The c.v. and the mean of the distance of fly from ceiling z. The solid and dashed lines represent c.v. and mean values, respectively. Different landing maneuvers are aligned in time at the beginning of pitch, which is defined as the moment when pitch rate reaches ¼ of the peak pitch rate. Time 0 represents the average touchdown time instant. The RREV calculated in $\mathcal{F}$ has the least c.v. compared with those in $\mathcal{F}_b$ and $\mathcal{F}_s$ frames, and also to those of the ω_x and ω_y. The c.v. of z is comparable to the RREV in $\mathcal{F}$, however since z cannot be directly measured by the flies, RREV is the most likely visual cue that triggers the body pitch maneuver.

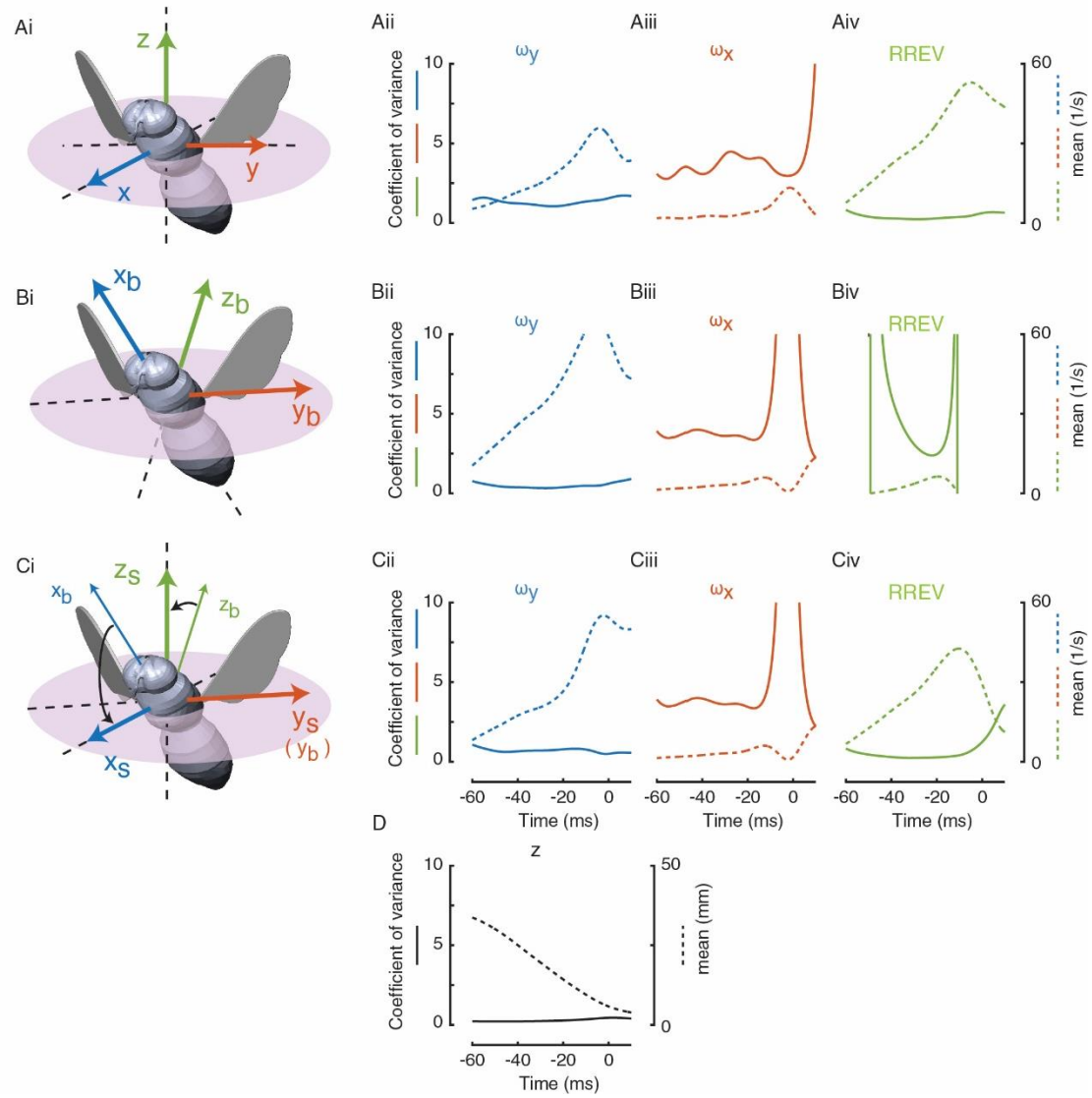

Fig. S5. The roll rotation in inverted landings is triggered when RREV exceeds a threshold. This figure displays the same information as those in fig. S4 except that the data from different landing trials are aligned at the start of roll. Again, the RREV calculated in yaw-aligned global frame $\mathcal{F} = \{x, y, z\}$ has the least coefficients of variance.

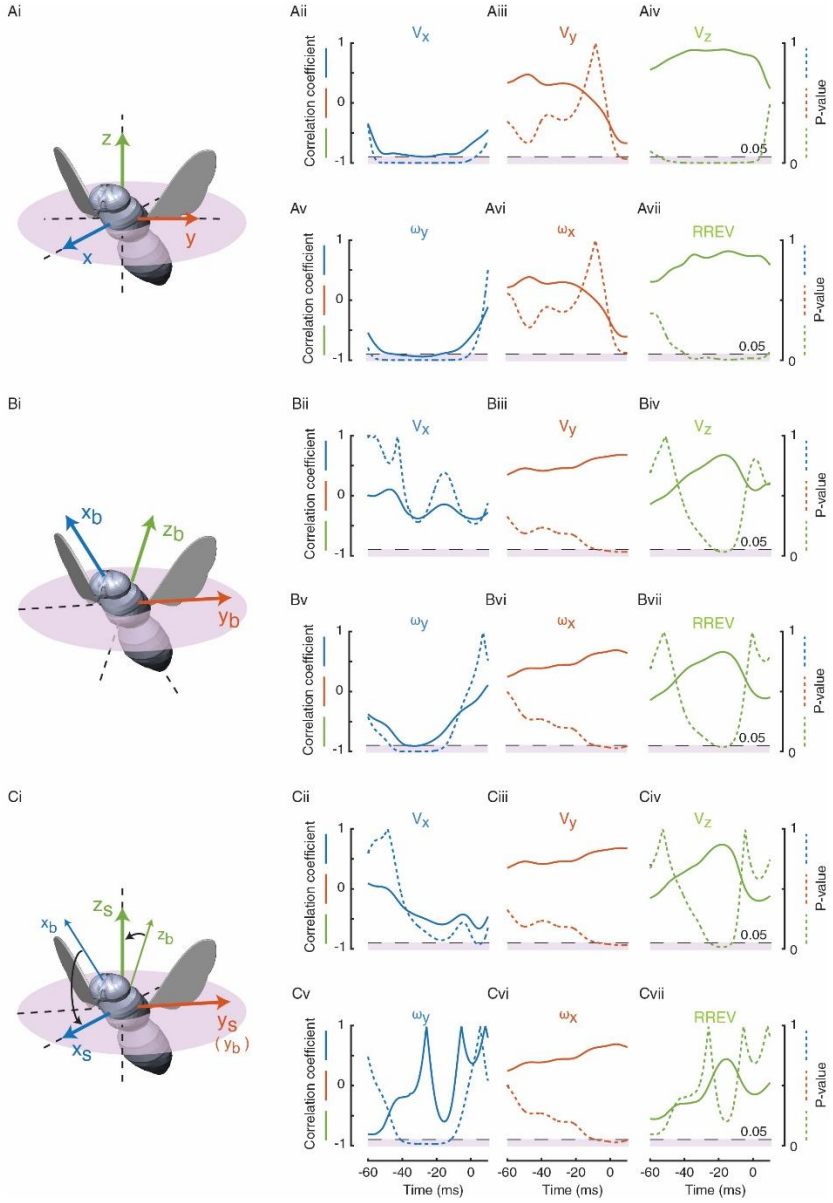

Fig. S6. Correlations between visual or mechanosensory cues to the pitch rate of the rotational maneuvers. Correlations of peak pitch rate with visual (ω_y, ω_x, and RREV) and mechanosensory (V_x, V_y and V_z) cues at different preceding time instants with respect to three sets of coordinate frames $\mathcal{F} = \{x, y, z\}$, $\mathcal{F}_b = \{x_b, y_b, z_b\}$ and $\mathcal{F}_s = \{x_s, y_s, z_s\}$ (successful landings, N =10) are shown. The solid and dashed lines represent the Pearson's linear correlation coefficients and P-value, respectively. The shaded area indicates P-value lower than 0.05. The data from different successful landing trials are aligned at the peak of pitch, and time 0 indicates the average time instant of feet touchdown on the ceiling. The peak pitch rate is positively correlated with both RREV and V_z, and negatively correlated with ω_y and V_x (in $\mathcal{F}$), but not with the sensory cues in $\mathcal{F}_b$ or $\mathcal{F}_s$, indicating that the $\mathcal{F}$ is the most likely coordinate frame in which the flies calculate the sensory cues.

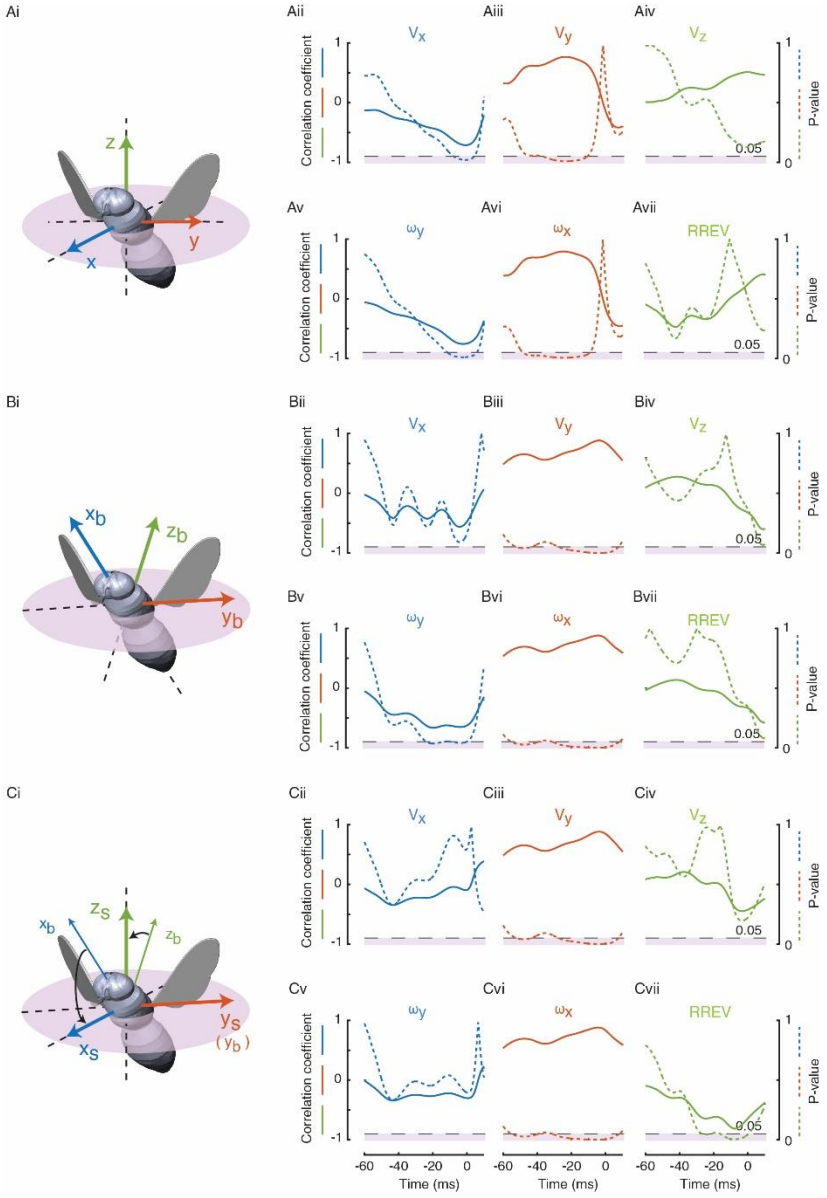

Fig. S7. Correlations between visual or mechanosensory cues to the roll rate of the rotational maneuvers. Correlations of peak roll rate with visual (ω_y, ω_x, and RREV) and mechanosensory (V_x, V_y and V_z) cues at different preceding time instants with respect to three sets of coordinate frames $\mathcal{F} = \{x, y, z\}$, $\mathcal{F}_b = \{x_b, y_b, z_b\}$ and $\mathcal{F}_s = \{x_s, y_s, z_s\}$ (successful landings, N =10) are shown. The figure shows the same information as those in fig. S6 except that data from different landing trials are aligned at the instant of peak roll rate. The peak roll rate is positively correlated with ω_x and V_y from all three coordinate frames. Note that there are only small differences between y, y_b and y_s in most trials of pitch-dominated landing.

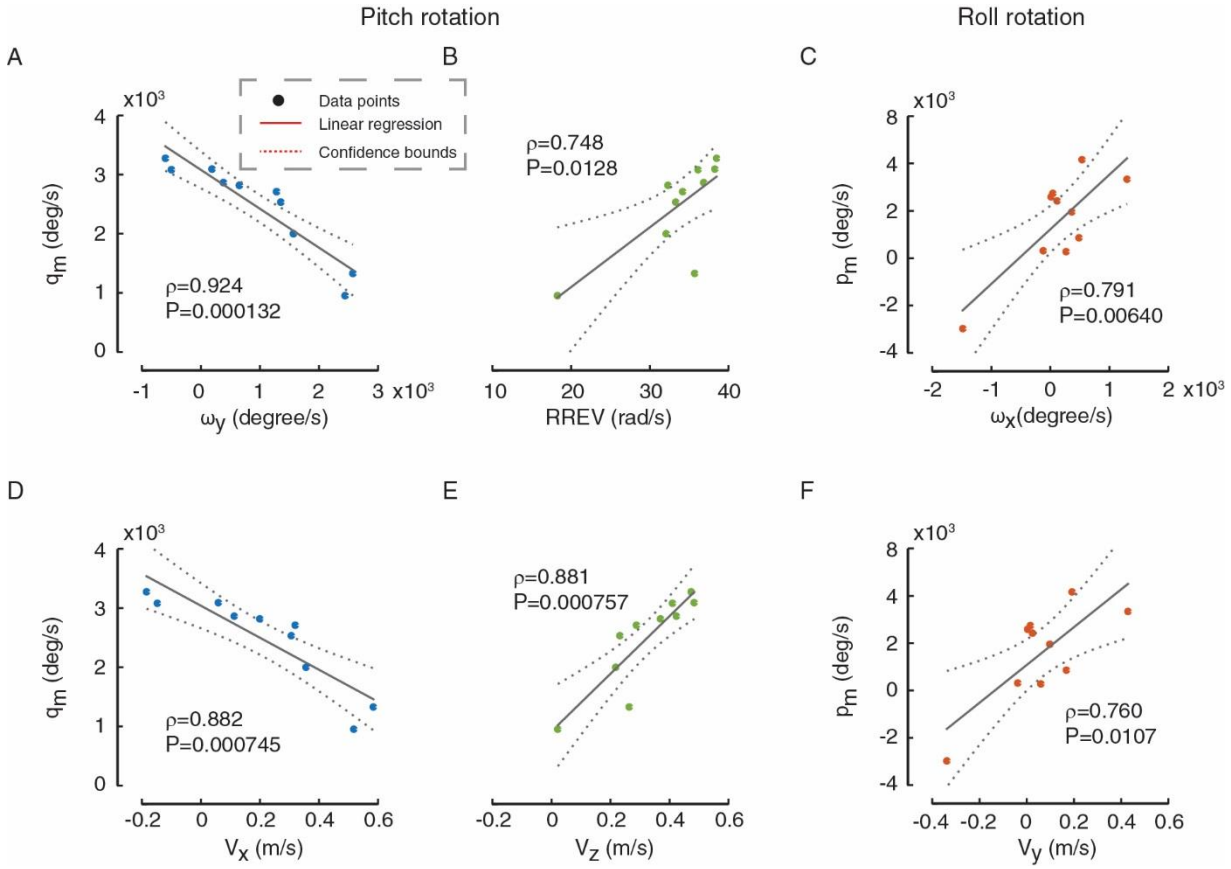

Fig. S8. Linear regressions between peak pitch (or roll) rate and sensory cues at an example time instant of 20 ms before the time instant of the peak pitch (or roll) rate. The sensory cues include visual cues: (**A**) ω_y, (**B**) RREV and (**C**) ω_x; and mechanosensory cues: (**D**) V_x, (**E**) V_z and (**F**) V_y. The q_m and p_m represent peak pitch and roll rate, respectively. The ρ and P are the correlation coefficient and P-value, respectively.

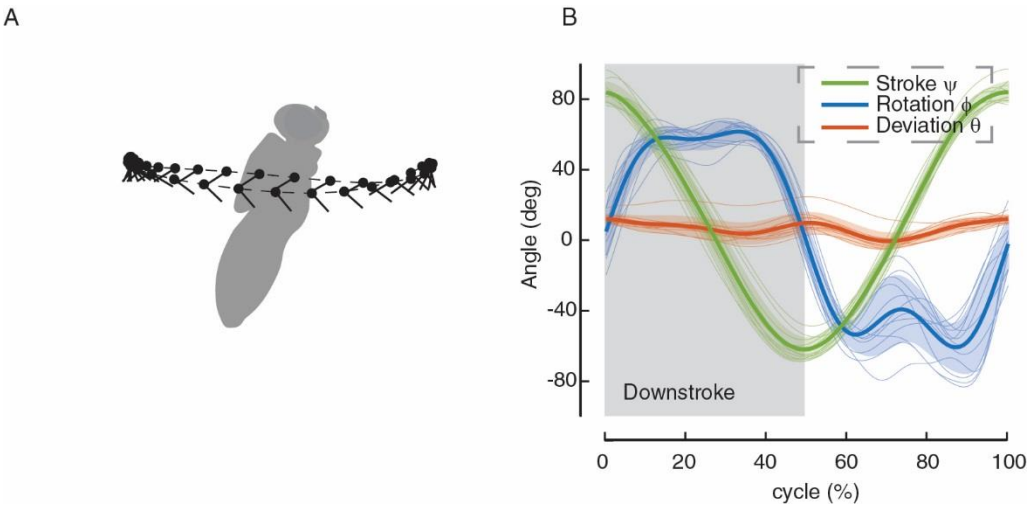

Fig. S9. The wing kinematics that generate upward acceleration prior to rotational maneuvers are defined as the reference wing kinematics. (**A**) Schematics of wing tip trajectory represented by the movements of a wing chord (black line). The black circle represents the leading edge. (**B**) Instantaneous wing kinematic angles within a time-normalized wingbeat cycle, including stroke angle ψ (green), rotation angle ϕ (blue) and deviation θ (red) angles. The thick and thin lines represent the averaged and individual wing kinematics, respectively. The shaded areas represent ± 1 s.d.

Table S1. Categorized landing trials. The inverted landing trials are categorized into (1) successful landing (landing in smooth and coordinated fashion in the first attempt), including: pitch dominated (PD), roll dominated (RD), longitudinal body swing dominated (SLon), lateral body swing dominated (SLat) and pitch-and-roll combined (PR); (2) landing with groping for the ceiling using forelegs (CG), and (3) failed landing due to early body rotation (FER), low body inversion with delayed leg extension (FDE), and low body inversion with minor body rotation (FMR). The number of digitized and analyzed trials for each category is listed. Note that after failed landing attempts, flies can always land successfully by groping for the ceiling using their forelegs, which occupied a large number of the trails we recorded, they are considered separately from the successful landing. The triggering and mediation of rotational maneuvers were analyzed based on the successful landing trials with the high-contrast perching area (total 13 trials), where 3 trials with a recording time less than 25 ms before the start of the rotational maneuver were discarded, resulting total 10 trials used in the analyses (fig. S8).

Landing types				Low contrast	High contrast	Total
Successful landing	Successful landing at the first attempt	PD	(Movie S1)	1	4	5
		RD	(Movie S2)	0	4	4
		SLon	(Movie S3)	2	1	3
		SLat	(Movie S4)	2	2	4
		PR	(Movie S5)	0	2	2
		Total		**5**	**13**	**18**
Groping	Groping landing after failed landing	CG	(Movie S6)	17	7	24
Failed landing	Failed landing attempts	FER	(Movie S7)	1	0	1
		FDE	(Movie S8)	0	5	5
		FMR	(Movie S9)	5	4	9
		Total		**6**	**9**	**15**

Table S2. The Pearson's linear correlation coefficient and *P* value between body rotation variables and multiple sensory cues at an example time instant of 20 ms before peak of rotation rate. The rotation variables include peak, average and integral of pitch, roll and yaw rate. The sensory cues include visual ω_y, ω_x and RREV and mechanosensory V_x, V_y and V_z.

Table S3. The Pearson's linear correlation coefficient and *P* value between body kinematic variables and the changes of wing kinematic variables. The body kinematic variables include stroke-averaged upward acceleration, pitch rate, roll rate, yaw rate, pitch acceleration, roll acceleration and yaw acceleration. The changes of wing kinematic variables include bilateral symmetric and asymmetric changes of stroke angle, wing rotation and deviation, stroke plane tilt and wingbeat frequency.

Movie S1. High-speed video recordings of an example pitch-dominated landing (PD) shown in Fig. 1D. The videos are from two side cameras operating at 5000 frames per second and are replayed at 30 frames per second, meaning that the videos are played 167 times slower than the real speed. Below the videos are the time traces of the corresponding linear and rotational kinematics and the visual cues. The time flow of the videos is represented by the moving vertical bars in each plot.

Movie S2. High-speed video recordings of an example roll-dominated landing (RD) shown in Fig. 1E. The setup of cameras, videos and the types of plots are the same as movie S1.

Movie S3. High-speed video recordings of an example longitudinal-body-swing-dominated landing (SLon) shown in Fig. 1F. The setup of cameras, videos and the types of plots are the same as movie S1.

Movie S4. High-speed video recordings of an example lateral-body-swing-dominated landing (SLat). The setup of cameras, videos and the types of plots are the same as movie S1.

Movie S5. High-speed video recordings of an example pitch-roll combined landing (PR). The setup of cameras, videos and the types of plots are the same as movie S1.

Movie S6. High-speed video recordings of an example landing with ceiling groping (CG). The setup of cameras, videos and the types of plots are the same as movie S1.

Movie S7. High-speed video recordings of an example failed landing due to early body rotation (FER) shown in fig. S2A. The setup of cameras, videos and the types of plots are the same as movie S1.

Movie S8. High-speed video recordings of an example failed landing due to low body inversion with delayed leg extension (FDE) shown in fig. S2B. The setup of cameras, videos and the types of plots are the same as movie S1.

Movie S9. High-speed video recordings of an example failed landing due to low body inversion with minor body rotation (FMR). The setup of cameras, videos and the types of plots are the same as movie S1.